



Atmosphere Origins for Exoplanet Sub-Neptunes

Edwin S. Kite¹ , Bruce Fegley Jr.², Laura Schaefer³ , and Eric B. Ford^{4,5,6,7}

¹ Department of the Geophysical Sciences, University of Chicago, Chicago, IL, USA; kite@uchicago.edu

² Planetary Chemistry Laboratory, McDonnell Center for the Space Sciences & Department of Earth & Planetary Sciences, Washington University, St. Louis, MO, USA

³ School of Earth Sciences, Stanford University, Palo Alto, CA, USA

⁴ Department of Astronomy and Astrophysics, The Pennsylvania State University, University Park, PA, USA

⁵ Center for Exoplanets and Habitable Worlds, The Pennsylvania State University, University Park, PA, USA

⁶ Institute for CyberScience, The Pennsylvania State University, University Park, PA, USA

⁷ Pennsylvania State Astrobiology Research Center, The Pennsylvania State University, University Park, PA, USA

Received 2019 October 28; revised 2020 January 19; accepted 2020 January 24; published 2020 March 11

Abstract

Planets with $2 R_{\oplus} < R < 3 R_{\oplus}$ and orbital period < 100 days are abundant; these sub-Neptune exoplanets are not well understood. For example, *Kepler* sub-Neptunes are likely to have deep magma oceans in contact with their atmospheres, but little is known about the effect of the magma on the atmosphere. Here we study this effect using a basic model, assuming that volatiles equilibrate with magma at $T \sim 3000$ K. For our Fe–Mg–Si–O–H model system, we find that chemical reactions between the magma and the atmosphere and dissolution of volatiles into the magma are both important. Thus, magma matters. For H, most moles go into the magma, so the mass target for both H_2 accretion and H_2 loss models is weightier than is usually assumed. The known span of magma oxidation states can produce sub-Neptunes that have identical radius but with total volatile masses varying by 20-fold. Thus, planet radius is a proxy for atmospheric composition but not for total volatile content. This redox diversity degeneracy can be broken by measurements of atmosphere mean molecular weight. We emphasize H_2 supply by nebula gas, but also consider solid-derived H_2O . We find that adding H_2O to Fe probably cannot make enough H_2 to explain sub-Neptune radii because $> 10^3$ km thick outgassed atmospheres have high mean molecular weight. The hypothesis of magma–atmosphere equilibration links observables such as atmosphere H_2O/H_2 ratio to magma FeO content and planet formation processes. Our model’s accuracy is limited by the lack of experiments (lab and/or numerical) that are specific to sub-Neptunes; we advocate for such experiments.

Unified Astronomy Thesaurus concepts: [Extrasolar rocky planets \(511\)](#); [Exoplanet atmospheres \(487\)](#); [Exoplanet evolution \(491\)](#); [Exoplanet formation \(492\)](#)

1. Introduction

Using exoplanet atmosphere data to constrain planet formation and evolution is a core goal of exoplanet research (Charbonneau et al. 2018). So far, most data have come from exo-Jupiters. However, smaller-radius worlds are far more intrinsically common (e.g., Hsu et al. 2019), and the characterization of their atmospheres is underway (e.g., Fraine et al. 2014; Knutson et al. 2014; Morley et al. 2017; Wakeford et al. 2017; Benneke et al. 2019). At $R < 4 R_{\oplus}$, most confirmed exoplanets are sub-Neptunes: worlds with $R = 1.6\text{--}3.2 R_{\oplus}$ and density < 4 g/cc (e.g., Rogers 2015; Wolfgang et al. 2016; Fulton et al. 2017). Sub-Neptunes probably have $10^3\text{--}10^4$ km deep H_2 -rich atmospheres cloaking rocky cores (e.g., Owen & Wu 2017; Van Eylen et al. 2018), at least for orbital period < 100 days. This implies that sub-Neptunes are mostly atmosphere by volume and mostly silicate by mass (Figure 1). Thus, we might expect that silicate–atmosphere interactions would set atmosphere mass and composition. Two (coupled) interactions matter most (Figure 1): the dissolution of the atmosphere into the magma and redox reactions involving atmosphere and magma (e.g., Hirschmann et al. 2012; Schaefer et al. 2016; Chachan & Stevenson 2018). Surprisingly, however, no previous study has investigated how these processes set atmosphere composition for sub-Neptunes.

What is the volatile content of sub-Neptunes, where did it come from, and where is it today? The most important volatile element is H. H on sub-Neptunes is stored as H_2 in the atmosphere, as H_2O in the atmosphere, as H_2 contained within

silicate (magma or rock; Chachan & Stevenson 2018), as H_2O dissolved in the silicate, and perhaps as H dissolved in Fe metal (e.g., Clesi et al. 2018). So far, sub-Neptune formation models have emphasized H stored in the atmosphere and H sourced from the nebula. This understates the H needed to produce an atmosphere of a given mass, ignores the possibility of H_2 generation via Fe oxidation (Rogers et al. 2011), and ignores H_2O generation by reduction of FeO (Sasaki 1990). New data from contaminated white dwarfs indicate extrasolar silicates with high FeO content (Doyle et al. 2019); reaction between such silicates and nebula gas would generate H_2O . Moreover, magma redox can probe planet formation (e.g., Urey 1952; Wänke 1981), and so atmospheric constraints on magma–atmosphere reactions and thus magma redox can probe planet formation (Figure 2).

We believe this is the first work on magma–atmosphere reaction for sub-Neptunes (for an overview of related solar system work, see Appendix E). Of previous related studies—e.g., Ikoma & Genda (2006), Rogers & Seager (2010), Rogers et al. (2011), Schaefer et al. (2016), Massol et al. (2016), Schaefer & Fegley (2017), and Ikoma et al. (2018)—the closest in intent to our own is that of Elkins-Tanton & Seager (2008a). Their study uses elemental mass balance to set upper limits on volatile abundance, but does not attempt to solve for redox equilibrium. Chachan & Stevenson (2018) use an ideal-gas model to study the solubility of H_2 in magma—the H_2 redox end-member in Figure 2. In Kite et al. (2019), we used a

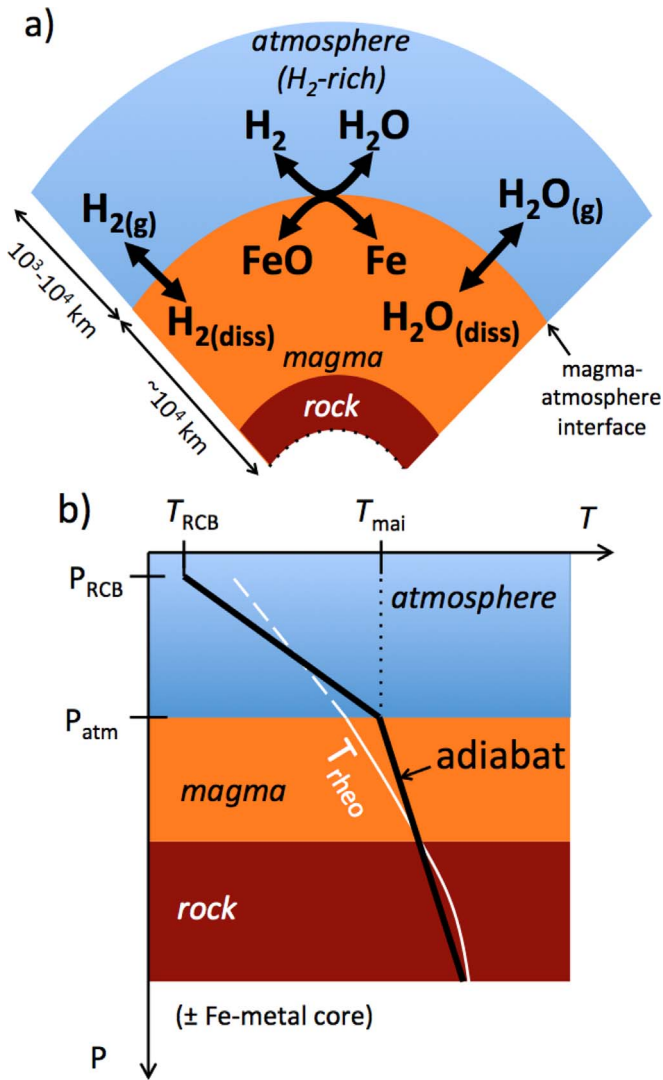


Figure 1. (a) Structure of *Kepler* sub-Neptunes assumed in this paper. For the first time, we model redox reactions between magma and atmosphere, specifically $\text{H}_2 + \text{FeO} \leftrightarrow \text{H}_2\text{O} + \text{Fe}$, on sub-Neptunes. (b) Temperature vs. pressure plot, showing adiabats within the atmosphere and the magma (black line). T_{rheo} (white line) corresponds to the temperature of the rheological transition ($\sim 40\%$ melt fraction) for rock. RCB = radiative-convective boundary. T_{mai} = temperature at the magma-atmosphere interface. For real sub-Neptunes, the equilibrium temperature (T_{eq}), the effective temperature (T_{eff}), and the temperature at the RCB (T_{RCB}) are related by $T_{\text{eq}} < T_{\text{eff}} \lesssim T_{\text{RCB}}$. In this paper, we make the approximation that these three temperatures are equal.

real-gas H₂ model to also study this end-member case, finding qualitatively different results from the ideal-gas model.

Because this is the first study of atmosphere-magma reaction for sub-Neptunes, in the remainder of this paper, we use a basic model (Section 2). We ignore photochemistry and fractionating escape to space (retention of O/H₂O versus loss of H). Results are given in Section 3. We emphasize applications and tests in our analysis (Section 4). We discuss in Section 5 and conclude in Section 6. Our main results are in Figures 7 and 8.

1.1. Most *Kepler* Sub-Neptunes Have Massive Magma Oceans in Direct Contact with the Atmosphere

Models show that an Earth-composition planet will double in radius if it gathers $\sim 3\%$ of its own weight into a nebula-

composition atmosphere (for orbital period ~ 10 days; e.g., Lopez & Fortney 2014; Bodenheimer et al. 2018). However, these models treat the remaining $\sim 97\%$ of the planet's mass (silicates plus Fe metal) as chemically inert. On the contrary, the magma-atmosphere interface on sub-Neptunes has a temperature (T_{mai}) hotter than the silicate liquidus, and the interface is chemically reactive and permeable (Schaefer & Elkins-Tanton 2018). T_{mai} is hot because *Kepler* sub-Neptunes form hot, and the atmosphere insulates the silicates. The sub-Neptune T_{mai} is much hotter than the sub-Neptune photosphere temperature T_{eff} . Pressure at the magma-atmosphere interface is 1–10 GPa (Figure 3).

The magma ocean forms a global shell underneath the atmosphere (Figure 1). This shell is most massive for young planets with thick atmospheres that are close to the star. T_{mai} versus time can be tracked with complex models (e.g., Howe & Burrows 2015; Chen & Rogers 2016; Bodenheimer et al. 2018; Vazan et al. 2018b). However, these studies all present T_{mai} for only a few cases, and with the exception of Vazan et al. (2018b), they do not estimate magma ocean mass. We wanted to build intuition for how magma ocean mass depends on T_{eff} and P_{atm} . Therefore, we wrote a toy model of sub-Neptune thermal structure (Appendix A). The toy model output is shown in Figure 3. The toy model indicates that for atmosphere mass down to 0.2 wt%, extensive magma occurs for $T_{\text{eff}} > 400$ K.

Above the liquidus, silicate magma is runnier than water, so if the magma layer convects, then the magma and atmosphere can stay equilibrated (Massol et al. 2016). In this paper, we assume full equilibration between the atmosphere and fully molten silicates. For this assumption to be correct, a necessary condition is that the silicates are fully molten. This condition is more likely to be satisfied for worlds that are young, retain thick atmospheres, and are in short-period orbits (high T_{eq}).

Magma is chemically potent. For example, the magma can be the host of most of the planet's exchangeable electrons (i.e., the magma can dominate the redox budget). This corresponds to planets with $O(1 \text{ wt}\%)$ atmosphere mass and $O(5 \text{ wt}\%)$ total volatile mass. We focus on this case here.

2. Method

To explore magma effects on sub-Neptune atmospheres, we assume the atmosphere equilibrates with a well-stirred magma ocean. Our model makes the following simplifications: (a) we consider only the elements Fe, Mg, Si, O, and H. Chemically reduced carbon compounds may also contain H; for simplicity, we omit consideration of them here. We also restrict ourselves to the range of magma elemental compositions for which SiO₂ is a major constituent. (b) We set $2000 \text{ K} \leq T_{\text{mai}} \leq 3000 \text{ K}$, so that the magma-atmosphere interface is molten but the vapor pressure of the magma is small relative to the total atmospheric pressure (Fegley et al. 2016; Sossi & Fegley 2018). This T_{mai} is at the low end of the T_{mai} output by thermal evolution models for multi-Gyr-old sub-Neptunes (e.g., Bodenheimer & Lissauer 2014; Howe & Burrows 2015; Vazan et al. 2018a). We consider lower T_{mai} in Section 4.4. (c) We ignore Fe³⁺ (i.e., Fe₂O₃). We expect Fe³⁺ will be a minor constituent of a magma ocean equilibrated with a H₂-dominated atmosphere. Equal thermodynamic activities of FeO and Fe₂O₃ in magma at 3000 K require $f_{\text{O}_2} = 28$ bar, much higher than expected from thermal dissociation of steam at any P and T below 1 kilobar and 3500 K. (d) We assume that metal (if present) is pure Fe for these calculations; in reality, the

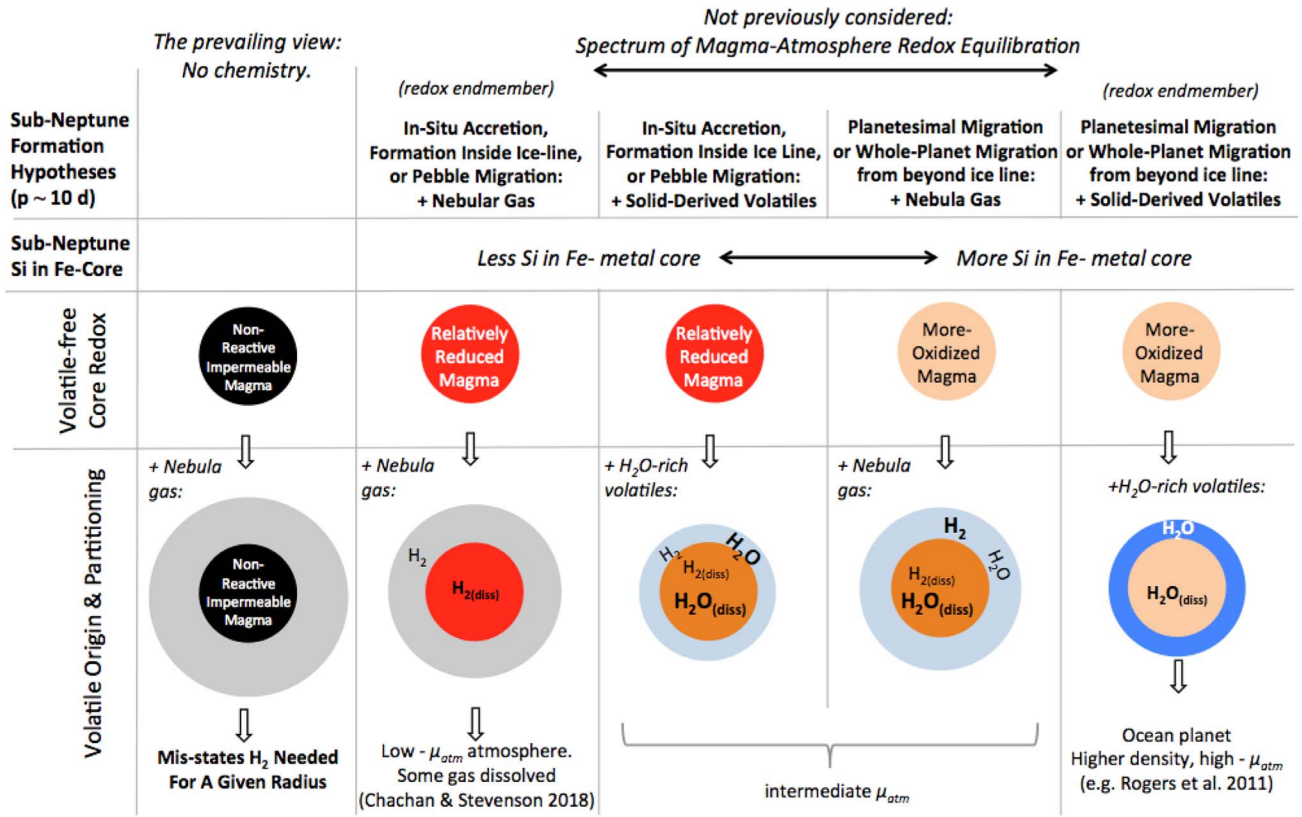


Figure 2. Magma-atmosphere interactions considered in this paper. μ_{atm} = atmospheric mean molecular weight; diss.= volatiles dissolved in magma. Magma oxidation may result from either net oxidation of the planet’s materials or dissolution of Si into the Fe-metal core (both processes might contribute; Appendix B).

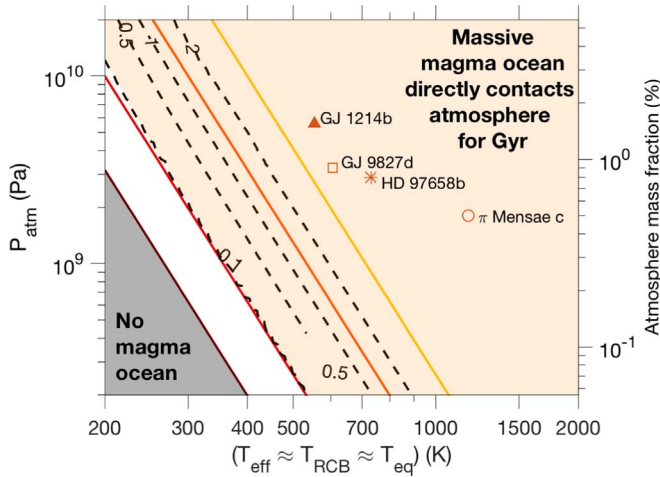


Figure 3. How magma ocean mass increases with atmospheric thickness. Output from a toy model of sub-Neptune thermal structure (Appendix A). Dashed lines correspond to magma ocean mass, labeled in Earth masses of magma, for a volatile-free planet mass of $5 M_{\oplus}$. Colored lines correspond to temperatures at the magma-atmosphere interface of (going from left to right) 1500, 2000, 3000, and 4000 K. Magma ocean masses in excess of 2 Earth masses are not plotted because this corresponds to a magma P range that is little explored by experiment. Planets of varying masses are overplotted: GJ 1214b (parameters from Nettelmann et al. 2011), GJ 9827d (Rice et al. 2019), HD 97658b (Dragomir et al. 2013/Van Grootel et al. 2014; upper limit on atmosphere mass), and π Mensae c (Huang et al. 2018).

metal will be an Fe-dominated alloy. We may be (slightly) underestimating fO_2 by doing this. (e) We track nonideal behavior of both H₂ and H₂O (Appendix C), but we assume ideal mixing of H₂ and H₂O. This is a valid assumption

both under mineral-free conditions in the atmosphere for $T > 650$ K, and also at the magma-atmosphere interface given our model assumptions (Seward & Franck 2019; Bali et al. 2013; Soubiran & Militzer 2015). We ignore joint-solubility effects. (f) We use a single value of gravitational acceleration g , corresponding to $1.2\times$ the bare-rock radius, to convert from bottom-of-atmosphere pressure to atmosphere column mass. (g) We ignore the effect of dissolved volatiles on core mass.

Consider a well-stirred magma ocean that is redox-buffered by the coexistence of liquid Fe metal and FeO-bearing magma:



The equilibrium constant for Reaction (1) is

$$K_1 = \frac{[\text{FeO}]^2}{[\text{Fe}]^2 fO_2} = \frac{[\text{FeO}]^2}{fO_2} \text{ for } [\text{Fe}] = 1. \quad (2)$$

The oxygen fugacity fO_2 corresponding to the coexistence of liquid Fe metal and liquid FeO is a function of T , P , and the chemical activity of FeO in the magma (Figure 4). Fugacity is a measure of chemical reactivity, expressed in units of pressure. Fugacity is $1\text{--}10\times$ the partial pressure of the gas for the range of conditions we consider (Appendix C). We obtain $fO_2(T, P)$ by combining data for the FeO liquid equation of state (EOS) of Armstrong et al. (2019) and for the Fe liquid EOS from Komabayashi (2014), assuming an activity coefficient for FeO (γ_{FeO}) of 1.5 (Holzheid et al. 1997). The Gibbs free energy at 1 bar for Reaction (1) is obtained from the data in Kowalski & Spencer (1995).

The resulting $fO_2(T, P)$ for the Fe/FeO buffer is shown in Figure 4. Both the fO_2 and the corresponding O_2 partial pressure are tiny compared to total atmospheric pressure

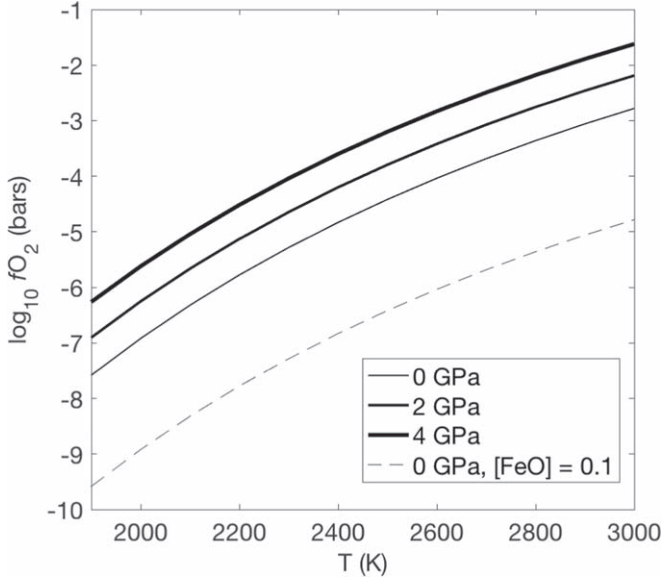
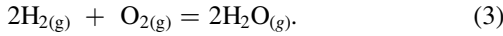


Figure 4. The oxygen fugacity, f_{O_2} , corresponding to the coexistence of liquid Fe metal and liquid FeO. The solid lines show the results for pure liquid FeO, and the dashed line shows the 100-fold reduction in f_{O_2} that results from reducing the concentration of FeO in the silicate magma to 10%.

(Figure 4). Thus, f_{O_2} is used in our model solely as a convenient bookkeeping variable for redox. The dominant atmospheric species in our model are H_2 and H_2O .

$f_{\text{O}_2} \propto [\text{FeO}]^2$, where $[\text{FeO}]$ is the activity of FeO in magma (e.g., Frost et al. 2008). Moreover, f_{O_2} is directly related to the $\text{H}_2/\text{H}_2\text{O}$ ratio in the atmosphere (Fegley 2013). The connection is the reaction



The equilibrium constant for Reaction (3) is

$$K_3 = \left(\frac{f_{\text{H}_2\text{O}}}{f_{\text{H}_2}} \right) \frac{1}{f_{\text{O}_2}}. \quad (4)$$

Using the equality of oxygen fugacity for Reactions (1) and (3), substituting, and rearranging then gives

$$\frac{[\text{FeO}]^2}{K_1} = \frac{1}{K_3} \left(\frac{f_{\text{H}_2\text{O}}}{f_{\text{H}_2}} \right)^2, \quad (5)$$

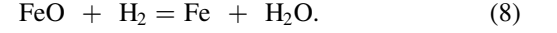
where $f_i = \phi_i P_i = \phi_i X_i P_{\text{total}}$, with ϕ_i a “fugacity coefficient” (Appendix C) and $P_i = X_i P_{\text{total}}$ is the partial pressure of the species with X_i the mole fraction, and

$$K_3 = \exp\left(\frac{-\Delta G^\circ}{RT}\right); \quad (6)$$

ΔG° increases by $\sim 120 \text{ kJ mol}^{-1}$ for a 1000 K rise in T . We use the expression

$$\begin{aligned} \Delta G^\circ(T) = & -4.8716 \times 10^5 + 94.261574 T \\ & + 9.9275922 \times 10^{-3} T^2 - 1.87633188 \times 10^{-6} T \\ & + 1.2446526 \times 10^{-10} T^4 \end{aligned} \quad (7)$$

(from the IVTAN Tables; Glushko et al. 1999). The net reaction is the sum of Reactions (1) and (3):



The equilibrium constant for Reaction (8) is

$$K_8 = \frac{[\text{Fe}]}{[\text{FeO}]} \frac{f_{\text{H}_2\text{O}}}{f_{\text{H}_2}} = \frac{1}{[\text{FeO}]} \frac{f_{\text{H}_2\text{O}}}{f_{\text{H}_2}} \text{ for } [\text{Fe}] = 1. \quad (9)$$

The equilibrium constant K_8 is equal to

$$K_8 = \left(\frac{K_3}{K_1} \right)^{1/2} = \frac{1}{[\text{FeO}]} \frac{f_{\text{H}_2\text{O}}}{f_{\text{H}_2}}. \quad (10)$$

This basic model (Equations (1)–(10)) shows that the atmosphere has a ratio of water to hydrogen that is proportional to the FeO content of the underlying magma. Thus, provided that no water clouds form in the cool upper layers of the atmosphere, spectroscopic constraints on O/H in the cool upper layers of the atmosphere probe the composition of deep magma.

Neither the atmospheric pressure nor the FeO content of the magma is a free parameter—both are results of magma–atmosphere equilibration. Therefore, we need to consider not just buffering of the atmosphere by the magma, but also the more general case of atmosphere–magma chemical coupling. Our approach to this is described below.

The H_2 solubility at the top of the magma layer is set to

$$X_{\text{H}_2} = 9.3 \times 10^{-12} f_{\text{H}_2} \exp(-T_0/1673), \quad (11)$$

where X_{H_2} is the mass fraction of H_2 in the melt, with $T_0 = 4000 \text{ K}$. This follows the estimated molten-average-rock solubility from Hirschmann et al. (2012; i.e., their estimated peridotite solubility). f_{H_2} is calculated from P_{H_2} using the procedure given in Appendix C. This solubility is $\sim 5\times$ lower than was used by Chachan & Stevenson (2018), who used a solubility for molten basalt. Our proposed temperature dependence of the H_2 solubility follows Chachan & Stevenson (2018). There are no direct measurements of H_2 solubility in liquid magma in the 2000–3000 K range.

The H_2O solubility at the top of the magma layer is approximated as (Schaefer et al. 2016)

$$\left(\frac{X_{\text{H}_2\text{O}}}{0.01} \right) = \left(\frac{P_{\text{H}_2\text{O}}}{241.5 \text{ MPa}} \right)^{0.74}, \quad (12)$$

where $X_{\text{H}_2\text{O}}$ is the mass fraction of H_2O in the melt. This expression is a curve fit to the results of Papale (1997) for basaltic melt; the high-pressure solubility of water in peridotite liquid is unknown.

Equilibration at the top of the magma layer sets volatile abundance throughout the well-stirred magma. This is because the solubility of volatiles goes up with depth within the magma. Therefore, saturation equilibrium at the magma–atmosphere interface implies subsaturated conditions at great depth (no bubbles and a constant mole fraction of H in magma). For a discussion of what happens if convection stalls, see Section 4.4.

Equipped with these solubilities and equilibrium constants, we then solve for the mass balance for H between H_2 in atmosphere, H_2 in magma, H_2O in atmosphere, and “ H_2O ” in magma. Our workflow is detailed in Appendix D.

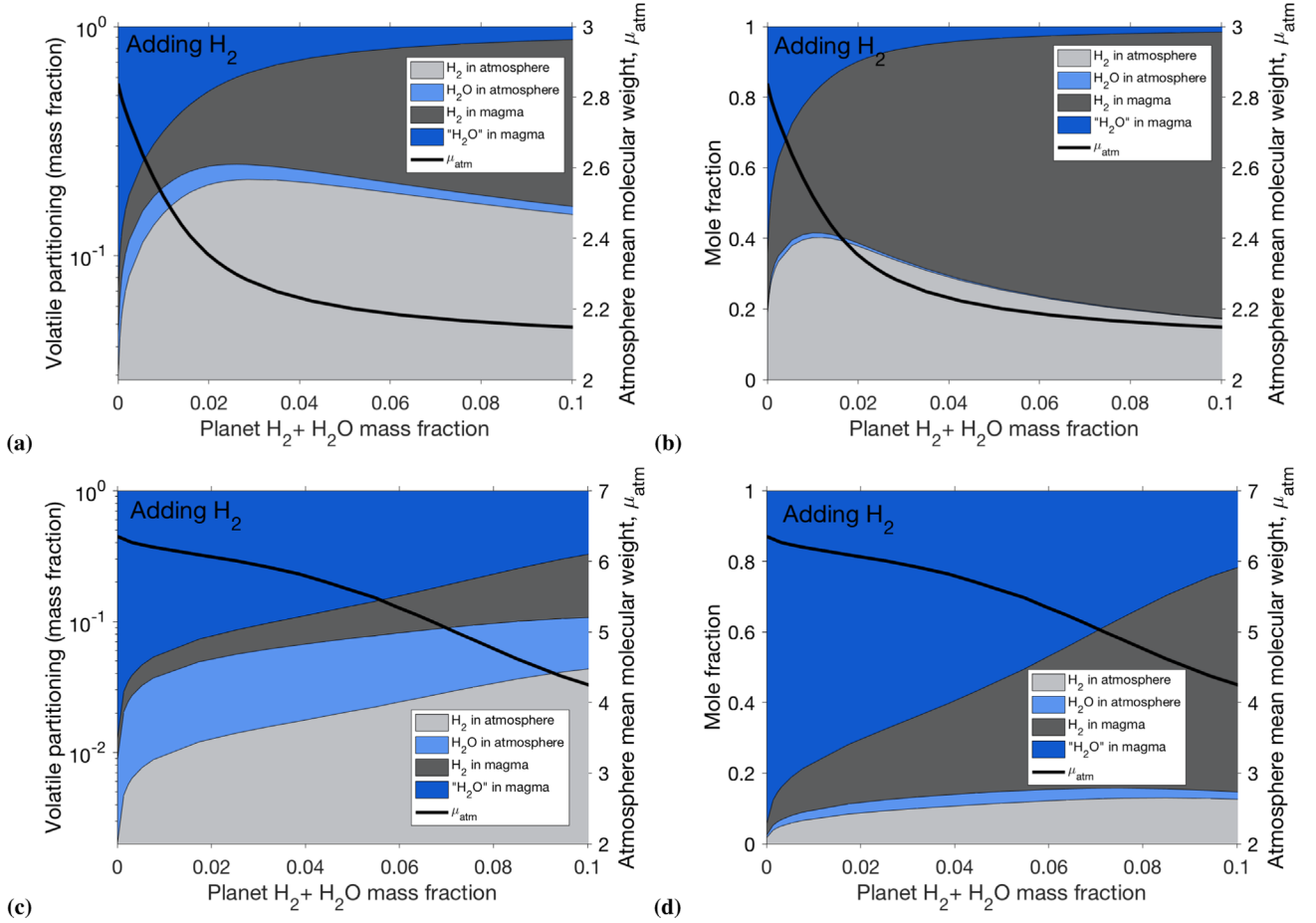


Figure 5. How magma composition controls the fate of H: adding H_2 to a magma ocean of $31/3$ Earth masses ($2/3$ of the mass of a 5 Earth mass planet) with a temperature at the magma–atmosphere interface (T_{mai}) of 3000 K. Simplified model (see text). For details, see Section 3.1. (a) and (b) show the consequences of adding varying amounts of nebular hydrogen to a planet with an initial Earth-like (8 wt%) FeO content in its magma. (a) shows mass fractions and (b) shows mole fractions. (c) and (d) show the consequences of adding varying amounts of nebular hydrogen to a planet with an initial FeO content in its magma similar to the mass of Fe oxide that would be obtained from completely oxidizing Earth’s mantle+core (49 wt%). This gives an FeO content similar to the most oxidized of the extrasolar silicate oxidation states reported by Doyle et al. (2019). (c) shows mass fractions and (d) shows mole fractions.

3. Results

3.1. Adding H_2 to an FeO-bearing Magma Ocean (Figure 5)

The top row in Figure 5 shows the consequences of adding varying amounts of nebula hydrogen to a planet with an initial Earth-like FeO content in its magma. Given our assumption of magma–atmosphere equilibration (discussed further in Section 5.2), the end results are the same if all of the nebula hydrogen is added after the core forms, or if the nebula hydrogen is added as the core is still growing.

Moving to the right on the x -axis of the plots in Figure 5 corresponds to adding volatiles to the planet. In Figure 5, the volatile we choose to add is nebula gas. Adding nebular gas is equivalent, in our Fe–Mg–Si–O–H system, to adding pure H_2 (we ignore O in nebula gas). As H_2 is added, H_2O is generated, via $\text{FeO} + \text{H}_2 \rightarrow \text{Fe} + \text{H}_2\text{O}$ (Ikoma & Genda 2006). Because (at relatively modest atmospheric pressure) H_2O is much more soluble in magma than is H_2 , the dominant reservoir for H is water dissolved in the magma. As H_2 is added, FeO goes to Fe, so f_{O_2} goes down, and the atmospheric $\text{H}_2\text{O}/\text{H}_2$ ratio goes down (it is proportional to $[\text{FeO}]$) (Figure 5). Thus, the atmospheric mean molecular weight decreases as H_2 is added.

Most H goes into the magma. H_2O stored in the magma (dark blue bands in Figure 5) can outweigh H_2 in the

atmosphere (light gray bands in Figure 5), even when the atmosphere is mostly H_2 . The importance of the magma as a volatile store is boosted by H_2 dissolution into the magma, corresponding to the dark gray bands in Figure 5 (Chachan & Stevenson 2018). The mass fraction of volatiles in the atmosphere peaks at <3 wt% (>97 wt% of volatiles are in the magma). It declines at higher P_{atm} because H becomes very soluble in magma at high P (Kite et al. 2019).

The lower row of Figure 5 shows the consequences of adding varying amounts of nebula hydrogen to a planet with an initial FeO mass fraction of 0.487 in its magma. This fraction corresponds to a planet for which Fe is initially entirely present as FeO. This planet does not have an Fe-metal core until H_2 is added (Elkins-Tanton & Seager 2008b). Even for an atmosphere corresponding to 3 wt% total volatiles, our initial FeO mass fraction = 0.487 world has a $\mu_{\text{atm}} \sim 6$ atmosphere (Figure 5(c)). This is because much of the nebular-sourced H_2 is oxidized to H_2O , and most of this H_2O is sequestered in the mantle.

Figure 5 shows that even modest magma oxidation has a big effect. We add nebula gas, but in the resulting planet, H_2O is very important (Figure 5). Adding H_2 to FeO makes H_2O , and H_2O is very soluble in magma. This is a redox-enabled hydrogen pump.

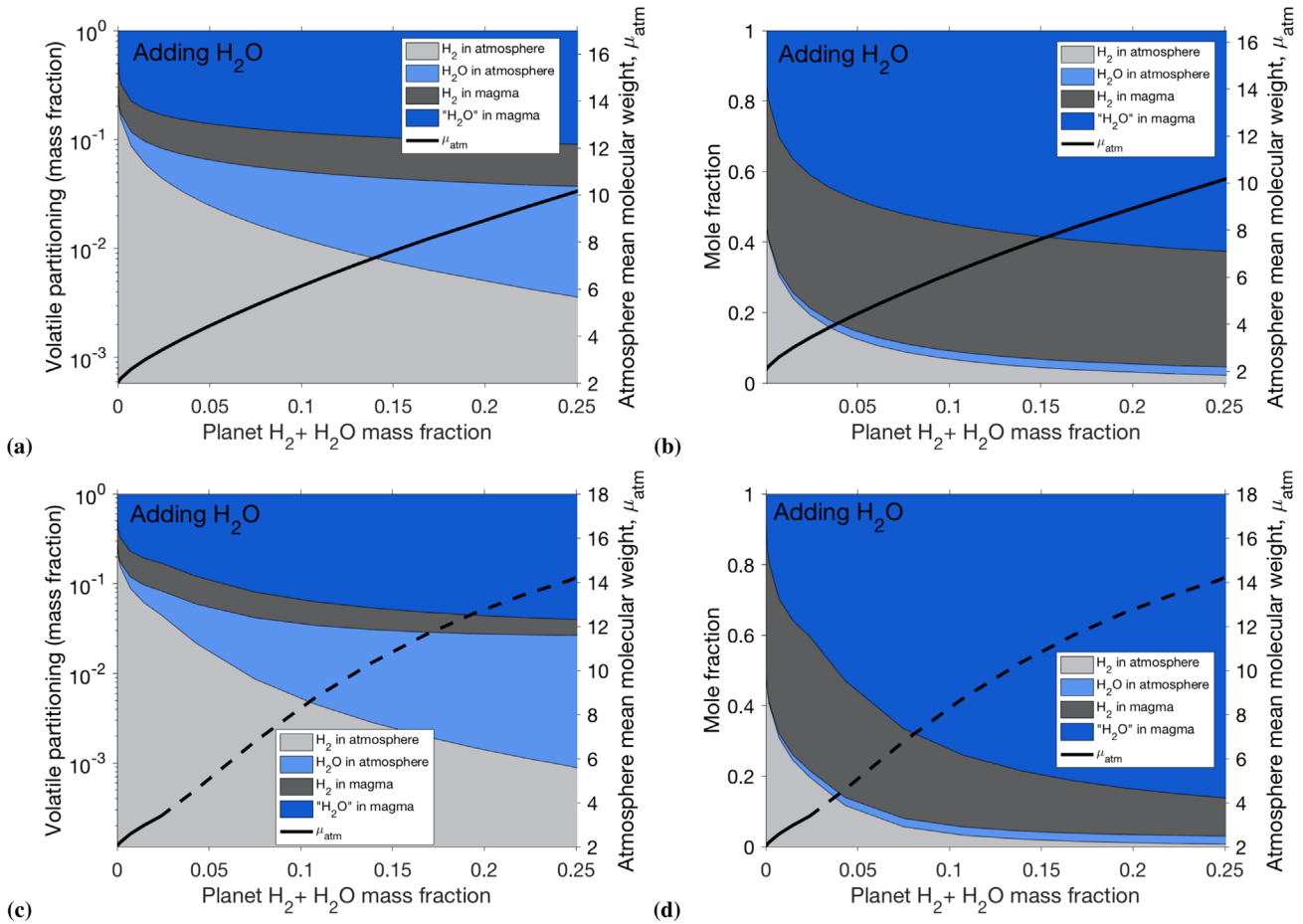


Figure 6. How magma composition controls the fate of H: adding H₂O to a magma ocean containing Fe metal. Simplified model. Temperature at the magma–atmosphere interface ($T_{\text{mai}} = 3000$ K. For details, see Section 3.2. (a) and (b) show the consequences of adding varying amounts of water to a planet with an initial dispersed Fe-metal content of 50 wt% in its magma ocean. (a) shows mass fractions and (b) shows mole fractions. (c) and (d) show the consequences of adding varying amounts of water to a planet with an initial dispersed Fe-metal content of 10 wt% in its magma ocean. The point where enough H₂O has been added to oxidize all of the Fe is shown by the transition from the thick black solid line to the thick black dashed line. (c) shows mass fractions and (d) shows mole fractions.

Real worlds apparently sample the full range of stoichiometrically possible silicate FeO contents. Within the solar system, silicate mantle FeO contents range from ≤ 0.04 wt% Fe⁽²⁺⁾O for Mercury (Nittler et al. 2017), to ~ 20 wt% Fe⁽²⁺⁾O for Vesta and Mars. Doyle et al. (2019) report extrasolar silicate oxidation states from contaminated white-dwarf spectra ($n = 6$). The highest of their values is roughly equivalent to the FeO content used in our full-oxidation calculation (Figure 5(c)).

The results in Figure 5 are for $T_{\text{mai}} = 3000$ K. If decreasing T_{mai} causes magma crystallization, then volatiles will be driven from the magma into the atmosphere—a big effect. For simplicity, we assume mantles are fully molten here. For a fully molten magma and fixed atmospheric pressure, the net effects of cooling T_{mai} from 3000 to 2000 K are relatively small.

Changing planet mass has little effect on the atmospheric composition in our model (for fixed atmospheric pressure and fixed, high T_{mai}). This is because R_{pl} is approximately proportional to $M_{\text{pl}}^{1/4}$ (we use $R_{\text{pl}}/R_{\oplus} = (M_{\text{pl}}/M_{\oplus})^{0.27}$; Valencia et al. 2006). Thus, gravity $g \propto M_{\text{pl}}^{1/2}$. Because atmospheric mass = PA_{mai}/g (where A_{mai} is the area of the magma–atmosphere interface), atmospheric mass is almost independent of planet mass for fixed P .

3.2. Adding Water to Fe-bearing Magma (Figure 6)

Could sub-Neptune atmospheres be the result of H₂ generation on the planet, with no need for H₂ delivery by nebula accretion? H₂ is generated when Fe metal reduces fluid H₂O (Elkins-Tanton & Seager 2008a; Genda et al. 2017; Haberle et al. 2019). This H₂O is ultimately derived from solids, for example, comets or hydrated asteroids.

Earth’s ocean could be destroyed 400 times over by reaction with Earth’s Fe-metal core (Lange & Ahrens 1984). Fortunately for life, most of the reducing power of Earth’s core is safely buried (Hernlund 2016). But is this true for exoplanets?

We do not know whether or not H₂ generation by Fe–H₂O reaction on sub-Neptunes is important. In this subsection, we set a new constraint on the atmosphere boost by this process, by showing how atmosphere mean molecular weight increases as H₂O is added to an Fe-bearing magma ocean. Here we build on previous stoichiometric calculations (Elkins-Tanton & Seager 2008a), by adding the requirement of thermodynamic self-consistency. To motivate this upper-bound calculation, we first speculate on some scenarios by which the Fe–H₂O reaction might occur. We do not attempt to calculate how closely these scenarios approach our thermodynamic upper bound. Because we find that our new thermodynamic constraint is restrictive enough that most sub-Neptune atmospheres

cannot be explained by Fe–H₂O reaction, the kinetics of these scenarios do not matter for the purpose of determining whether or not most sub-Neptune atmospheres can be explained by Fe–H₂O reaction.

Routes by which Fe might encounter H₂O on a sub-Neptune include the following. (1) If most of the Fe-metal mass is delivered in the form of pebbles or planetesimals, then Fe-metal-bearing pebbles or planetesimals will vaporize in the atmosphere (e.g., Brouwers et al. 2018), permitting chemical equilibration with the atmosphere. (2) Small embryo impacts disperse Fe metal through the magma ocean, increasing the chance that Fe metal and H₂O can react (Deguen et al. 2014). (3) Giant impacts can yield iron fragments, whose reaccretion promotes H₂ generation (Genda et al. 2017). (4) For sufficiently energetic giant impacts, the boundaries between Fe-metal core, silicate magma, and the atmosphere become blurry (Stevenson 1984). This physical boundary-blurring may favor chemical equilibration.

Results for adding water to a magma ocean initially containing 50 wt% Fe metal (intermediate between the bulk-planet Fe content of Earth and the bulk-planet Fe content of Mercury) and with initially negligible FeO are shown in Figures 6(a) and (b). Results for adding water to a magma ocean initially containing 10 wt% Fe metal and initially negligible FeO are shown in Figures 6(c) and (d). (10 wt% Fe metal in the magma ocean might correspond to emulsification of the impactor after a giant impact onto proto-Earth.) H₂ is initially generated, but as the H₂O supply increases, the atmosphere molecular mass increases. Dissolved H₂O in magma is the dominant volatile reservoir. The results for different mantle Fe-metal contents are identical up to an atmosphere mass of ~ 0.01 Earth masses. Above that point, the two tracks diverge. This is because, for the 10 wt% Fe-metal case (Figures 6(c) and (d)), all Fe metal has been converted to FeO. In our model framework, no more H₂ can be generated. Adding more H₂O simply dilutes the H₂ generated by Fe+H₂O \rightarrow FeO+H₂. This dilution zone is shown by dashed lines in Figures 6(c) and (d) and corresponds to fast increase of atmosphere mean molecular weight. By contrast, for the 50 wt% Fe-metal case, the reaction Fe+H₂O \rightarrow FeO+H₂ continues to release new H₂ into the atmosphere. This slows the rise to high atmosphere mean molecular weight.

Why is the composition of the first-produced atmosphere independent of the Fe content for the “H₂O added to Fe-bearing magma ocean” case, while the composition depends on FeO content for the “H₂ added to oxidized magma” case? This is because FeO exists as part of a liquid solution in the silicate magma (with MgO and SiO₂), whereas liquid Fe metal is a pure phase in our model (Anderson 1996). As a result, the no-volatiles $f\text{O}_2$ depends on the *abundance* of FeO for an Fe-free magma, but for an FeO-free magma, the no-volatiles $f\text{O}_2$ depends only on the *existence* of Fe.

4. Analysis

4.1. The Fraction of Volatiles that are Stored in the Magma is Variable, and This Decouples Radius from Composition (Figure 7)

For H₂-dominated atmospheres, sub-Neptune radius is a proxy for atmospheric mass (Lopez & Fortney 2014). However, radius is not a proxy for total volatile mass if the atmosphere equilibrates with a massive magma ocean

(Figure 7). This is because of the variable dissolution of H in the magma (as H₂ and as “H₂O”).

To see that dissolution matters, consider a planet where the volatile-free FeO content of the magma is the same as that of Earth. Starting from a volatile-free world and adding H₂ until the atmosphere mass is 0.7 wt%, we find that $3\times$ more moles of H must be added than would be necessary in the absence of magma-atmosphere interaction (Figure 5(b)). This factor of 3 difference is near the low end of our model predictions. Factor of 50 (sic) enhancements are possible (Figure 7).

To illustrate that atmospheric mass is not a good predictor of total volatile mass, we first make two restrictive assumptions. (1) Nebular gas provides all volatiles. (2) The range of magma FeO contents (prior to any volatile addition) varies between planets, from [FeO] = 0 wt%, up to that of Earth’s [FeO], 8 wt%. These two assumptions confine us to the triangular region between the thick black line and the solid blue lines in Figure 7(a). The uncertainty in total volatile mass (for a given atmosphere mass) is a factor of $\gtrsim 10$. Moreover, if we drop either of our two restrictive assumptions, then the uncertainty explodes. Mars and Vesta both have [FeO] ≈ 20 wt%, and white-dwarf data suggest exoplanet silicate [FeO] up to ~ 50 wt% (Doyle et al. 2019). If [FeO] can range from 0 wt% to 48.7 wt%, then the uncertainty rises to a factor of ~ 20 (the range between the thick black line and the dashed blue lines in Figure 7(a)). Alternatively, let us drop restrictive assumption (1). In this case, the volatiles could be predominantly derived from solids (Figure 7(b)). For complete equilibration between magma and volatiles, the results are confined to the region between the gray dotted line and the dashed/solid lines in the lower right of Figure 7(b). But incomplete equilibration (or partial freeze-out) allows the planet to span the full range of parameters shown in Figure 7(b). The corresponding uncertainty is a factor of ~ 100 .

Our analysis implies the following:

1. Current theory (e.g., Ginzburg et al. 2016; Venturini & Helled 2017; Lee et al. 2018) understates the amount of H that must be added to turn a rocky super-Earth-sized planet into a sub-Neptune by a factor of $\gtrsim 3$, for a well-stirred deep magma ocean with an initial FeO content equal to that of Earth rocks (Figure 5).
2. Escape processes used to explain the conversion of sub-Neptunes into rocky super-Earth-sized planets (Owen 2019) must be more efficient by a factor of >3 for a well-stirred deep magma ocean with an initial (prior to H₂ addition) FeO content equal to that of Earth rocks. Magma stays equilibrated with the atmosphere as atmosphere is lost, so atmosphere losses will be mostly replaced by exsolution (Figure 7; Schaefer et al. 2016).
3. If magma redox states are diverse (Doyle et al. 2019), then some close-in planets with radii in the super-Earth range will have a H₂-rich atmosphere. This is a novel prediction, for the following reason. A H₂-rich atmosphere must be thin (<0.05 wt% of planet mass) for a $\geq 5 M_{\oplus}$ planet to remain in the super-Earth radius range. To explain such a thin atmosphere, fine-tuning of H inventory would be needed using the nonreactive impermeable magma approach. However, our model shows that such an atmosphere can correspond to 0.05–7 wt% total volatile mass. With redox diversity, no fine-tuning of H inventory is needed to give a H₂-rich atmosphere for planets with radii in the super-Earth range. This prediction can be tested

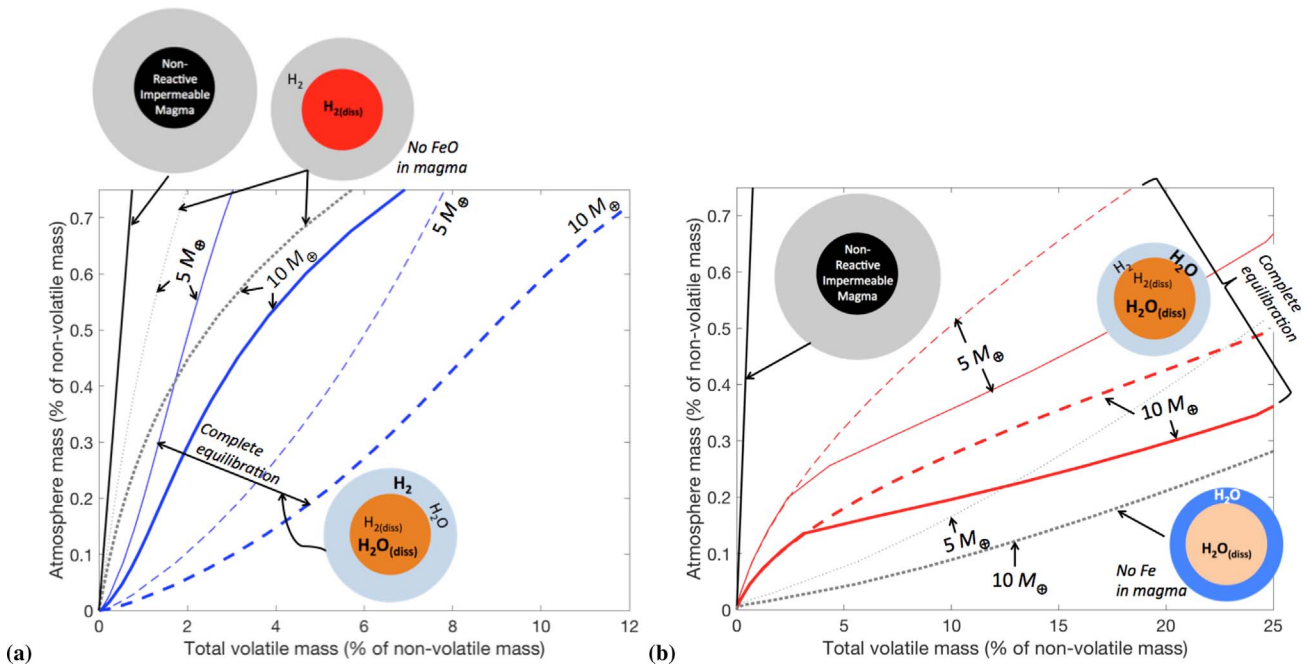


Figure 7. Atmosphere mass as a function of total volatile mass. When the core is chemically nonreactive and impermeable, all volatiles are in the atmosphere (thick solid black line). (a) Blue lines show the results for adding H_2 to magma with initial FeO content of 8 wt% (solid lines) or 48.7 wt% (dashed lines). As a set, the extrasolar silicate oxidation states reported by Doyle et al. (2019) plot closer to the dashed lines than to the solid lines. Line thicknesses correspond to planet (silicate + metal) mass: thin for $5 M_\oplus$, thick for $10 M_\oplus$. Because H_2O is more soluble than H_2 , the reaction $\text{FeO} + \text{H}_2 \rightarrow \text{Fe} + \text{H}_2\text{O}$ suppresses planet radius inflation—magmatic “ H_2O ” acts as a hydrogen sump. The gray dotted lines correspond to a very reduced core (negligible FeO); in this case, H is partitioned between dissolved H_2 and H_2 in the atmosphere (no H_2O). (b) Red lines show results for adding H_2O to a magma ocean with Fe content of 10 wt% (solid lines) or 50 wt% (dashed lines). Because H_2 is less soluble than H_2O , the reaction $\text{Fe} + \text{H}_2\text{O} \rightarrow \text{FeO} + \text{H}_2$ acts to boost the atmosphere relative to the reference case (which is shown by the gray dotted lines). This reference case corresponds to an Fe-metal-free magma ocean. For details, see Section 4.1.

with ARIEL (Tinetti et al. 2016) and perhaps the *James Webb Space Telescope* (at HR 858; Vanderburg et al. 2019; or at GJ 9827c; Rice et al. 2019).

4.2. Measurements of Atmosphere Mass and Mean Molecular Weight Can Probe Atmosphere Origins (Figure 8)

Sub-Neptune formation is not well understood. We do not know how rocky cores grow—giant impacts or pebble/planetesimal accretion (e.g., Chatterjee & Tan 2014; Levison et al. 2015)? We do not know where the growth happened—formation in situ or planet migration (e.g., Chiang & Laughlin 2013; Lee 2019; Mordasini 2018)? We do not know where the volatiles came from—nebula gas or solid-derived volatiles?

These hypotheses make distinct predictions for the mean molecular weight of the atmosphere (μ_{atm}) and the atmosphere mass/planet mass ratio (f_{atm}). Both can potentially be constrained by observations (e.g., Benneke & Seager 2012; Fortney et al. 2013; Benneke et al. 2019). Within our model, for $T_{\text{eff}} > 400$ K sub-Neptunes, we make the following connections (Figure 8):

Ⓐ *High $\text{H}_2\text{O}/\text{H}_2$ ratio (much greater than solar) \rightarrow planetesimal or planet migration, or Si dissolution into Fe-metal core.* A high $\text{H}_2\text{O}/\text{H}_2$ ratio in the atmosphere (much greater than solar) indicates the magma is oxidized. Oxidized magma can be produced either by net oxidization of the planet’s materials, or by rearrangement of oxidizing power inside the planet (with a net transfer of reductants to the Fe-metal core leaving oxidants in the silicate mantle; see Appendix B). Net oxidation of a planet’s materials involves a contribution to the planet’s building blocks from beyond the water-ice snow line—either planet migration or planetesimal migration. This is

because the easiest way to oxidize a planet’s building blocks is the reaction $\text{Fe}_{(\text{s})} + \text{H}_2\text{O}_{(\text{l})} \rightarrow \text{FeO}_{(\text{s})} + \text{H}_{2(\text{g})}$, followed by escape of H_2 to space (Appendix B). Thus, magma oxidation should (for an ensemble of planets) increase with semimajor axis (Rubie et al. 2011, 2015; Appendix B). This tendency is seen in the solar system: Mercury’s mantle has ≤ 0.04 wt% $\text{Fe}^{(2+)}\text{O}$ (Nittler et al. 2017), Earth’s has ~ 8 wt% $\text{Fe}^{(2+)}\text{O}$, Mars’ has 18 wt% $\text{Fe}^{(2+)}\text{O}$, and Vesta’s mantle has ~ 20 wt% $\text{Fe}^{(2+)}\text{O}$. If (near-)resonant chains of planets record more migration than planetary systems that lack such chains, then systems with (near-)resonant chains of planets should have magma oceans that are more oxidized.

The Si-dissolution mechanism predicts that planets that formed hotter (i.e., bigger planets) will tend to have magmas that are more oxidized (Fischer et al. 2017) (Appendix B).

Ⓑ $\mu_{\text{atm}} > 7 \rightarrow$ *large-object migration.* Sub-Neptune atmospheres cannot reach $\mu_{\text{atm}} > 7$ by reactions between magma and nebula gas (Figure 8). Instead, gas from solid-derived volatiles (H_2O , C-species, etc.) is needed. Because the ice lines for these solid-derived volatiles are at orbital period $> 10^2$ days, $\mu_{\text{atm}} > 7$ implies inward migration of objects that are large enough to resist dry out during migration (Bitsch et al. 2019). Atmospheres formed by reacting liquid Fe-metal with solid-derived volatiles plot in the red region in Figure 8. Atmospheres derived directly from solid-derived volatiles can also plot in this region. The two options might be distinguished by probing for C species. C species are extremely Fe loving (Dasgupta & Grawal 2019), so if atmospheres interact with liquid Fe metal, then C species should be absent. Liquid iron scrubs C from the atmosphere.

Ⓒ $\mu_{\text{atm}} < 7$, *plus atmosphere mass $> 0.03 M_\oplus \rightarrow$ nebula accretion.* Points in Figure 8 that are within the blue zone,

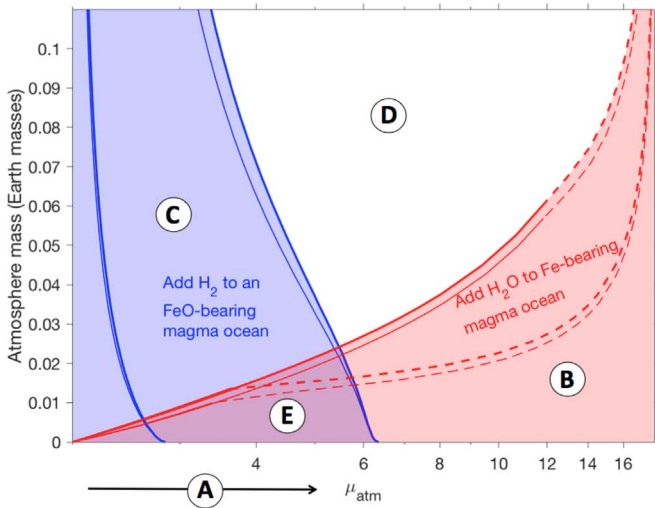


Figure 8. Effect of magma–atmosphere reactions on sub-Neptune atmosphere mass and atmosphere mean molecular weight (simplified model, at magma–atmosphere interface temperature $T_{\text{mai}} = 3000$ K, assuming a well-mixed H_2/H_2 atmosphere). Thin lines: $M_{\text{pl}} = 5 M_{\oplus}$, thick lines: $M_{\text{pl}} = 10 M_{\oplus}$. Arrow (A) corresponds to the increase in μ_{atm} from atmosphere reactions with an oxidized core, or from supply of solid-derived volatiles. Red zone (B) corresponds to adding H_2O -rich solid-derived volatiles to an Fe-bearing magma ocean. Blue zone (C) corresponds to adding nebular gas to an FeO-bearing magma ocean. Adding nebular gas to a magma ocean with the FeO contents inferred for extrasolar silicates from white-dwarf spectra by Doyle et al. (2019) would yield atmospheres in the right-hand half of the blue zone. White zone (D) is water-buffered. Purple zone (E) corresponds to ambiguous atmospheric origins. The leftmost pair of blue lines corresponds to an Earth-like volatile-free mantle FeO content. The rightmost pair of blue lines corresponds to a volatile-free mantle FeO content of 48.7 wt%. The leftmost pair of red lines corresponds to a magma ocean that has 50 wt% Fe metal in the volatile-free limit. The rightmost pair of red lines corresponds to a magma ocean that has 10 wt% Fe metal in the volatile-free limit. The point where enough H_2O has been added to oxidize all of the Fe corresponds to the transition from the red solid lines to the red dashed lines. We did not model Fe^{3+} , but if we had, then both the colored zones would slightly expand. For details, see Section 4.2.

above the red line, can only be formed by nebular accretion (not generation of H_2 by Fe– H_2O reactions). Within this region, upper limits on μ_{atm} (from the amplitude of features in transmission spectra) place upper limits on the [FeO] content of magma, and/or the extent of atmosphere–magma interaction. This is because planets with a higher volatile-free magma FeO content, or that have a greater degree of atmosphere–magma equilibration, plot farther to the right within the blue zone on Figure 8.

(D) Water-buffered worlds. Atmospheres that plot in the white zone in Figure 8 cannot be explained by gas release by the reaction of arriving material with the magma. These worlds likely gathered a major contribution from H_2O .

(E) Zone of overlap = ambiguous origins. Thin atmospheres with $2 < \mu_{\text{atm}} < 7$ can be explained either by endogenic generation of H_2 or by nebular accretion. Thin atmospheres can also be explained by high-molecular-weight volcanic outgassing, as on Earth, Venus, and Mars.

Figure 8 relates the mass, and the mean molecular weight, of sub-Neptune atmospheres to two key parameters. The first parameter is the magma redox state. The second parameter is the number of H atoms contained within the sub-Neptune. Both parameters can constrain models of planet formation.

In the future, further constraints might come from D/H data, where D/H values that are elevated (relative to the D/H of the

host star) point toward a greater contribution from solid-derived volatiles (Morley et al. 2019).

4.3. Endogenic H_2 Cannot Explain Most Orbital-period <100 Day Sub-Neptunes

Can the radii of sub-Neptunes be explained by H_2 generated on the planet (endogenic H_2)? This is (just) possible if every Fe atom gives up all three redox-exchangeable electrons to form H_2 from H_2O (Elkins-Tanton & Seager 2008b; Rogers & Seager 2010; Rogers et al. 2011). In that case, up to 3.6 wt% H_2 will be generated. For H_2 , 3.6 wt% is sufficient to account for most sub-Neptune radii, if all H_2 resides in the atmosphere. However, most of the H_2 will dissolve into the magma (Figure 7). Moreover, our model shows that adding H_2O will lead to a high-molecular-mass atmosphere ($\mu > 8$) for atmosphere mass > 0.8 wt% of planet mass (Figure 8). Therefore, endogenic H_2 cannot explain most orbital-period <100 day sub-Neptunes. Nebula gas is needed.

4.4. Trends over Gyr: Puff-up versus Late Ingassing

Existing models predict that sub-Neptunes will shrink with age as they cool and lose mass (e.g., Lopez & Fortney 2014; Vazan et al. 2018a). Magma–atmosphere equilibration makes different predictions. These predictions can be tested by comparing radius data for planets that differ in age. The needed data are now becoming available (e.g., Silva Aguirre et al. 2015; Johnson et al. 2017; Mann et al. 2017; David et al. 2019; Newton et al. 2019).

Puff-up: As planets cool and/or lose H_2 to space, the magma ocean can freeze (Figure 3). The magma–atmosphere interface is not the first layer to freeze. Rather, the freezing starts at great depth (e.g., Bower et al. 2019). When magma starts to freeze, volatiles are excluded from the solid and are strongly enriched in the residual melt. The volatile-enriched melt forms bubbles, which burst at the magma–atmosphere interface. Magma ocean freezing will squeegee volatiles into the atmosphere (Elkins-Tanton 2011).

Volatiles are pistoned into the atmosphere (leading to bigger radii than predicted by existing models) on the freeze-out timescale (billions of years; e.g., Vazan et al. 2018a). This puff-up effect depends on semimajor axis (because shorter-period worlds will never freeze) and on atmospheric thickness (because thickly blanketed worlds will never freeze). Puff-up predicts a statistical excess of sub-Neptunes in the diagonal band between 2 Earth masses of magma and 0.1 Earth masses of magma on Figure 3. This prediction might be tested with *TESS* mission extensions, or *PLATO* (European Space Agency 2013).

Late Ingassing: Consider a sub-Neptune with a H_2 atmosphere that is initially out of equilibrium with an FeO-rich magma ocean. This might occur if the magma is initially stratified (no convection), and the H_2 accretes only after the magma+metal core is assembled. In this scenario, the deeper magma will stay volatile free until the uppermost part of the magma ocean cools enough for the magma to convect (timescale $\gtrsim 10^9$ yr; Vazan et al. 2018a). Once convection starts, the planet will shrink. This is because (1) H_2 will dissolve into the magma, and (2) as the atmosphere is progressively oxidized, it becomes more soluble. Late ingassing predicts a shrinkage excess relative to existing models.

H₂O generation by the redox reactions could slow the cooling of planets with nebular-derived atmospheres. This is because H₂O is a major source of radiative opacity.

5. Discussion

5.1. Approximations and Limitations

5.1.1. Material Properties

Our material properties are mostly extrapolated from $T < 2000$ K lab data. At higher temperatures, they could be in error (e.g., Fegley & Schaefer 2014; Fegley et al. 2016; Sossi & Fegley 2018). For example, we ignore the T dependence of H₂O solubility. This dependence is weak (for Si-poor magmas) at $T < 2000$ K (Fegley & Schaefer 2014). More lab experiment and/or numerical experiment data (e.g., Soubiran & Militzer 2015) for material properties (especially solubility of volatiles in silicate) at the T and P of magma–atmosphere interfaces on sub-Neptunes are critically needed.

Our H₂O solubility model is for dissolution in basaltic magma because high-pressure data for peridotite magma is not available. H₂O solubility in magma increases dramatically with total pressure, and water and (peridotitic) magma are fully miscible above 3–6 GPa (Shen & Keppler 1997; Ni et al. 2017). Nonlinear H₂O solubility at much lower pressures interpolates between the solubility at low water content (for which H₂O is dissolved mainly as OH[−] and \sqrt{P} solubility is a good match to data; Abe & Matsui 1986; Pöhlmann et al. 2004; Karki et al. 2010), and the solubility at high water content (for which H₂O is increasingly dissolved as molecular H₂O; Stolper 1982). The fO_2 dependence of H₂O solubility is weak for Fe³⁺-absent conditions (Bolfan-Casanova et al. 2002), and we ignore it.

5.1.2. Composition

If we had tracked carbon instead of just hydrogen (Bitsch et al. 2019), then adding solid-derived volatiles would have produced a quicker increase in μ_{atm} .

Our toy model of magma ocean mass uses melting curves reported for a “chondritic mantle” composition with minimal volatiles (Andraut et al. 2011). This composition can be thought of as average solar system rock (Unterborn et al. 2017; Putirka & Rarick 2019). Including the effect of volatiles on the melting curve would favor melting, and so increase magma ocean mass (Katz et al. 2003). On the other hand, reported volatile-free pyrolite melting curves are at higher T than for chondritic mantle (Andraut et al. 2017); switching from a chondritic mantle melting curve to a pyrolite melting curve would reduce magma ocean mass.

We ignore Fe³⁺ (Kress & Carmichael 1991; Frost et al. 2004; Zhang et al. 2017). Including Fe³⁺ would modestly increase the compositional effect of magma–atmosphere interaction. Therefore, our omission of Fe³⁺ is conservative.

5.1.3. Thermodynamic Treatment

We ignore H storage by dissolution into liquid Fe metal (Stevenson 1977; Clesi et al. 2018; Wu et al. 2018). If this reservoir is large, then that would strengthen our conclusion that only a fraction of the H supplied from the nebula stays in the atmosphere.

We omit helium. Helium may slightly decrease H₂ solubility in melt, but because of helium’s small mole fraction in nebular gas, this is unlikely to be a big effect.

For the atmosphere, we use the Lewis–Randall approximation. In other words, we ignore the fact that the fugacity coefficient of a gas in a mixture is different from that of the pure gas, due to the molecular interactions in the gas mixture.

For our Fe–FeO buffer calculations, in effect we assume the partial molal volume of FeO in magma is independent of the magma Si content. Our assumed partial molal volumes for FeO are from measurements on melts that have more Si than for plausible sub-Neptune magma ocean compositions (Armstrong et al. 2019). This is probably not a big effect.

Thermal dissociation of H₂ to atomic H is minor for our purposes. At 3000 K and 10⁸ Pa, the H/H₂ molar ratio is just ~0.5%, dropping further at higher pressures.

5.2. How Long for Magma–Atmosphere Equilibration?

Our calculations assume that magma–atmosphere equilibration happens during planet formation. We do not know whether or not this assumption is correct. This assumption is plausible if magma oceans grow by giant impacts (e.g., Inamdar & Schlichting 2015), and each giant impact energetically stirs the growing planet. The equilibrium assumption is also plausible if magma oceans grow by condensation and rain-out of solids that were vaporized upon accretion (e.g., Bodenheimer et al. 2018; Brouwers et al. 2018). However, this planetesimal- or pebble-accretion scenario might give rise to a stably stratified magma ocean, with hot H-rich layers overlying deeper rock layers that are H poor and cooler because they equilibrated with lower-pressure atmospheres earlier in planet growth history. Such an onion-shell structure would have less H₂ dissolved in the magma, and (for a nebula volatile source) less H₂O in the atmosphere, than for our default model. Finally, the magma ocean might form volatile poor if silicate cores reach full size in an environment that has a low base-of-atmosphere pressure (e.g., Ormel et al. 2015). In this last case, convection is needed for nonnegligible equilibration (Pahlevan et al. 2019). Dissolution of volatiles into magma decreases the density of magma (Ochs & Lange 1999), an effect whose sign is to stabilize magma layers near the top of the magma ocean (disfavoring convection). Convection will cease if the stabilizing buoyancy from gradients in volatile abundance with depth exceeds the destabilizing buoyancy from planet cooling. Even if convection continues, the volatile-enriched boundary layer is thinner than the thermal boundary layer (because the diffusivities of H and OH are less than the thermal diffusivity). This slows regassing.

There is another way to suppress magma convection. At sufficiently high temperature, iron, melt, and volatiles become fully miscible. In this limit, magma and atmosphere are indistinguishable—a single phase. For example, water and (peridotitic) magma are fully miscible above 3–6 GPa (Ni et al. 2017). In the context of planet formation, full miscibility at high T suggests a zone of intermediate density (Helled & Stevenson 2017; Bodenheimer et al. 2018; Brouwers & Ormel 2020). Such a rock–volatile fuzzy zone has recently been discovered on Jupiter (Wahl et al. 2017). As fuzzy zones cool, the temperature gradient favors convection, but the compositional gradient inhibits convection. For H₂/magma fuzzy zones, it is not clear whether or not convection can continue (a review of the relevant fluid mechanics problem is given in Garaud (2018); parameterizations of the consequences

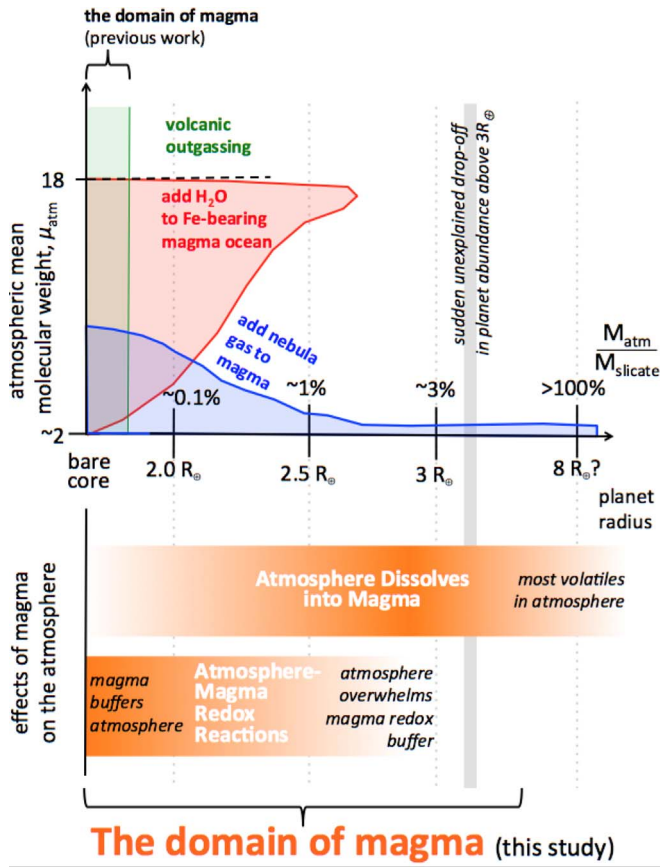


Figure 9. Conclusions in context. We found that both magma–atmosphere redox reactions and atmosphere dissolution into magma can be important for setting atmospheric composition. For very massive atmospheres, the redox buffer is overwhelmed, but dissolution of atmosphere in magma is very important (Kite et al. 2019). At sufficiently high planet radius, the atmosphere greatly outweighs the silicates and the atmosphere is little affected by the silicates. For atmosphere mass $\ll 0.1$ wt% of planet mass, volcanic outgassing (not considered in this paper) may explain atmospheres. The bottom line is that our work expands the range of atmosphere compositions and atmosphere masses that can be explained by atmosphere interactions with magma.

of sluggish or stalled convection for planet thermal evolution include that of Leconte & Chabrier (2012), and French & Nettelmann (2019) calculate the crucial Prandtl number (albeit for H_2O). If convection stalls and does not restart, then magma–atmosphere equilibration will effectively stop.

6. Conclusions

We draw five main conclusions from our simplified model.

1. Magma matters (Figure 9). Sub-Neptune atmosphere composition and mass can be greatly affected by atmosphere–magma interaction (Figures 2–6). For worlds that are mostly magma by mass, atmosphere $\text{H}_2\text{O}/\text{H}_2$ records both volatile delivery (exogenic water) and also volatile–magma interactions (which may produce endogenic water). The need to consider endogenic water complicates interpretation of atmosphere metallicity measurements (e.g., Mordasini et al. 2016). Atmosphere metallicity measurements have already been made for Neptune-sized exoplanets (e.g., Fraine et al. 2014; Crossfield & Kreidberg 2017; Morley et al. 2017; Wakeford et al. 2017; Turrini et al. 2018; Benneke et al. 2019, 2019) and will soon be extended to

sub-Neptunes. Interpretation of atmospheric metallicity on sub-Neptunes will not be a simple extension of theory developed for gaseous planets.

2. A lot of H goes into the magma (Chachan & Stevenson 2018; Figures 5–7). Boosting the radius of a magma-cored sub-Neptune requires more H_2 than is usually assumed. For example, if sub-Neptune silicates have a volatile-free magma FeO content similar to that inferred for extrasolar silicates on the basis of white-dwarf spectra (Doyle et al. 2019), then $>4\times$ more H_2 must be added to explain a given sub-Neptune’s radius.
3. Turning a sub-Neptune into a rocky super-Earth-sized planet requires more H loss than is usually assumed. This is because H loss is compensated by exsolution from the magma. Bubbling is a negative feedback on atmospheric loss. The corresponding increase in the demand for H loss (to explain a given radius change) pushes hypothesized H -loss mechanisms closer to their energetic upper limits. This extra demand may stress-test H -loss models such as core-powered mass loss (Ginzburg et al. 2018), impact erosion (Inamdar & Schlichting 2016; Zahnle & Catling 2017; Biersteker & Schlichting 2019), and photoevaporation (Owen & Wu 2017).
4. Atmosphere mass and atmosphere mean molecular weight can be used as a proxy for atmosphere origin (Figure 8). Atmosphere $\text{H}_2\text{O}/\text{H}_2$ ratio is proportional to magma FeO content.
5. If the magma and the atmosphere equilibrate, as is assumed by our model, then there are consequences we can test (Kite et al. 2019). One example is a statistical excess of sub-Neptunes with $\sim 10^{25}$ kg magma oceans (Section 4.4).

Our model is limited by the lack of material property data (e.g., solubilities) from lab and/or numerical experiments for the conditions at the sub-Neptune magma–atmosphere interface ($T > 2000$ K, $P = 1\text{--}10$ GPa). The effects that we have uncovered are big, so such lab and/or numerical experiments are strongly motivated if we are to understand what lies at the heart of sub-Neptune composition and evolution.

E.S.K. conceived research. E.S.K. and B.F. designed research. E.S.K. carried out the work, with contributions from B.F. (fugacity coefficients) and from L.S. (Fe–FeO buffer values), and E.S.K. wrote the paper, with a contribution (Appendix C) from B.F. All authors contributed to editing the paper.

Everything used to make this paper can be obtained for unrestricted further use by e-mailing the lead author.

We thank an anonymous reviewer for useful comments. We thank Paul Asimow, Andy Campbell, Dan Fabrycky, Greg Gilbert, Marc Hirschmann, Nadia Marounina, Miki Nakajima, Megan Newcombe, Dave Stevenson, and Sarah Stewart for discussions. We thank Kaveh Pahlevan for feedback on a draft. This work was supported by the U.S. taxpayer, primarily via grant NNX16AB44G (NASA) and secondarily via grant NNX17AC02G (NASA) and grant AST-1517541 (NSF). E.B.F. acknowledges support from the Center for Exoplanets and Habitable Worlds, which is supported by The Pennsylvania State University, the Eberly College of Science, and the Pennsylvania Space Grant Consortium.

Appendix A Magma on Sub-Neptunes

Rock with the composition of average Earth rock starts to melt at 1350 K and is mostly molten by 1750 K (Katz et al. 2003). Sustaining such high temperatures (for orbital period >3 days) requires an atmospheric blanket (Ikoma & Genda 2006). To find the atmospheric-blanket thickness, we first note that the most important constituent of the deep (convecting) atmosphere of sub-Neptunes is molecular hydrogen, H_2 . We use an adiabatic index for H_2 , γ , of $4/3$, which is appropriate for our pressure (P) and temperature (T) of interest (Saumon et al. 1995). Then, for an ideal gas we have

$$\left(\frac{T_{\text{mai}}}{T_{\text{RCB}}}\right) = \left(\frac{P_{\text{atm}}}{P_{\text{RCB}}}\right)^{\frac{\gamma-1}{\gamma}} \approx \left(\frac{P_{\text{atm}}}{P_{\text{RCB}}}\right)^{0.25}, \quad (13)$$

where “mai” denotes the magma–atmosphere interface and “RCB” denotes the boundary between the radiative outer atmosphere and the convecting (adiabatic) deep atmosphere (Figure 1). Equation (13), with $P_{\text{RCB}} = 10$ bar, gives us the colored curves in Figure 3. We assume that the planet’s internal luminosity is small compared to insolation, but is still large enough that the radiative zone is small. Thus, $T_{\text{RCB}} \approx T_{\text{eff}}$ (effective temperature) $\approx T_{\text{eq}}$ (equilibrium temperature).

To obtain the mass of the magma (the dashed lines in Figure 3), we must consider another effect: under pressure, magma will freeze. To track pressure-freezing, we used Figure 3 in Andraut et al. (2011) to get the $T(P)$ for the 100% melt curve (the liquidus), the 0% melt curve (the solidus), and magma adiabats. We interpolated linearly in temperature for intermediate melt fractions. (The liquidus and solidus both curve significantly at high pressure and are almost parallel to the adiabat around 10^2 GPa; Bower et al. 2018; Miyazaki & Korenaga 2019.) This gave us a relationship between P and melt fraction for a range of T_{mai} . (We assume that the temperature difference between the top of the magma and the lower layers of the atmosphere is small.) To map P onto the depth within the silicate interior of sub-Neptunes, we assumed the relationship between pressure and density for the Earth’s silicate mantle (from Dziewonski & Anderson 1981; magma densities are up to 15% lower; Bower et al. 2019). We integrated the pressure downward from the top of the magma, assuming that the distance from the center of the planet to the magma–atmosphere interface R_{mai} is given by

$$\left(\frac{R_{\text{mai}}}{R_{\oplus}}\right) = \left(\frac{M_{\text{pl}}}{M_{\oplus}}\right)^{0.27} \quad (14)$$

(Valencia et al. 2006), where M_{pl} is planet mass.

Above $T_{\text{mai}} = 3000$ K, a mostly or fully molten mantle is a reasonable approximation for sub-Neptune mass $\leq 4 M_{\oplus}$ (Figure 3). This result is specific to the melting curves reported by Andraut et al. (2011).

The atmosphere thermal blanket effect is much more important than pressure-freezing from the weight of the atmosphere. As a result, the dashed lines in Figure 3 are nearly parallel to the T_{mai} contours.

Magma ocean mass depends strongly on T_{mai} , but only weakly on planet mass. For thin magma shells, $M_{\text{magma}} \propto A/g$, $M_{\text{magma}} \propto M_{\text{pl}}^{0.08}$ from Equation (14). This near-cancellation of the gravity effect and the area effect is also seen in models of crust/lithosphere mass, e.g., Kite et al. (2009). For thicker

magma shells, geometric corrections produce a faster increase of magma ocean mass with planet mass.

The magma configuration on sub-Neptunes—with a global magma layer directly in contact with the atmosphere—is similar to that on terrestrial planets immediately after a giant impact (Elkins-Tanton 2012; Hamano et al. 2013). The sub-Neptune magma configuration is very different from that on tidally heated rocky worlds such as Io (which have a magma or silicate–mush layer under a solid rock layer). The sub-Neptune magma configuration is also very different from that on magma planets with silicate vapor atmospheres, which (in the absence of tidal heating) have a superficial (<100 km deep) dayside magma pool overlying solid rock (Léger et al. 2011; Kite et al. 2016). Sub-Neptune magma oceans are intrinsically much more abundant than magma planets (Winn et al. 2018; Hsu et al. 2019), long-lived (e.g., Vazan et al. 2018b), and massive (Figure 3). It is possible that sub-Neptunes contain most of the magma in the universe.

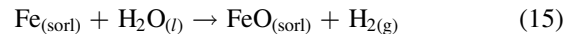
Appendix B How Magma Gets Oxidized

Protoplanetary disks with solar composition are very reducing because the H/O ratio is so large that the equilibrium fO_2 is about six orders of magnitude below that of the iron–wüstite buffer. FeO-bearing silicates and magnetite are thermodynamically stable only at such low temperatures (≤ 600 K for FeO-bearing silicates, ≤ 400 K for magnetite) that their formation may be kinetically inhibited (Krot et al. 2000; Lewis 2004; Grossman et al. 2012).

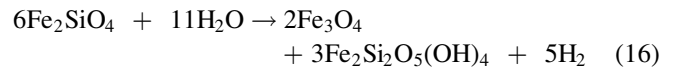
Nevertheless, copious FeO is found in rocky-planet silicates (Righter & O’Brien 2011). How do silicates get oxidized? One possibility is net loss of H_2 from the planet (or from the planet’s building blocks). The other is rearrangement of oxidizing power inside the planet, with a net transfer of reductants to the Fe-metal core leaving oxidants in the silicate mantle. These two mechanisms can work in concert (Fischer et al. 2015). It turns out that loss of H_2 from the planet is expected if the planet’s mass includes a large contribution from components that grew to kilometer-size or larger outside the H_2O –ice snow line. Rearrangement of reducing power inside the planet is expected if an Fe-metal core equilibrates with silicate at high temperature, as is likely on $\gtrsim 1 M_{\oplus}$ planets.

Oxidation mechanism 1: Net loss of reducing power from the whole planet.

The reaction



occurred on solar system planetesimals (Zolensky et al. 1989, 2008; Rosenberg et al. 2001; Castillo-Rogez & Young 2017). Another route to Fe oxidation is during the hydration of Fe silicates (alongside Mg-silicates) at $T < 800$ K. For example,



(“serpentinization”; Sleep et al. 2004; McCollom & Bach 2009; Klein et al. 2013). For $R < 10^3$ km objects, the gravitational binding energy for H_2 molecules is not much greater than their thermal energy for H_2 molecules. Thus, Reactions (15) and (16) on planetesimals and small embryos cause the return of H_2 to the nebula (e.g., Le Guillou et al. 2015), and rock oxidation

(Wilson et al. 1999; Rosenberg et al. 2001; Brearley 2006). Planets that form by collision between such preoxidized chunks can themselves be very oxidizing.

Indeed, meteorites are much more oxidizing than the nebula (Doyle et al. 2019). Meteorite-based models of outgassing output high-molecular-weight atmospheres (Schaefer & Fegley 2010). Solar system rocky planet $\text{H}_2/\text{H}_2\text{O}$ ratios are $\ll 1$ and correspond to $\log f\text{O}_2$ between approximately the iron (Fe)–wüstite (FeO) oxygen fugacity buffer (the “IW buffer”) and the more-oxidizing quartz (SiO_2) – fayalite (Fe_2SiO_4) – magnetite (Fe_3O_4) oxygen fugacity buffer (the “QFM buffer”). So, redox disequilibrium between nebula and magma, with the magma being more oxidized, is widespread in the solar system.

We do not know how widespread these processes are in the Galaxy. Oxidation states inferred for extrasolar planetesimals based on white-dwarf data fall within the range for solar system silicates (Doyle et al. 2019). Generation of H_2 on diameter $< 10^3$ km bodies in the solar system via Reaction (15) is aided by ^{26}Al decay. To the extent that the solar system acquired a high dose of ^{26}Al , the solar system might be a biased sample (Lichtenberg et al. 2019, but see also Young 2020).

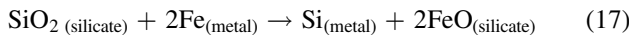
Neither Reaction (15) nor Reaction (16) can operate on pebbles, because liquid water requires pressures > 600 Pa (the triple point of H_2O), which is much more than the pressure in a pebble. Planets that grow by pebble accretion can generate H_2 by Reaction (15), but if they are large enough to retain the H_2 generated by these reactions, they might end up very reducing.

The connection between pebble accretion and sub-Neptune atmospheric composition that we are proposing only works if pebbles are not fragments of much larger bodies. Suppose instead that pebbles are dominantly debris from collisions between planetesimals. In this case, neither Reaction (15) nor Reaction (16) could have taken place within planetesimals that were then broken up to make pebbles.

Kepler sub-Neptunes are inside the H_2O snow line. Whole-planet oxidation involves a contribution to the planet from beyond the H_2O snow line. This could involve planet migration (e.g., Cossou et al. 2014; Ogihara et al. 2015; Izidoro et al. 2017; Kite & Ford 2018; Raymond et al. 2018; Carrera et al. 2019). Alternatively, an oxidized sub-Neptune core could be assembled at its current location from planetesimals that migrated.

Oxidation mechanism 2: Rearrangement of reducing power inside the planet.

At high temperature, Si can dissolve into liquid metal at wt% levels via the reaction



(Javoy 1995; Fischer et al. 2015). Reaction (17) oxidizes the mantle. It is effective at oxidizing the mantle if fewer than two O atoms dissolve into the Fe metal for every Si atom that dissolves into the Fe metal. This condition is satisfied when the mantle is reduced. (This redox dependence suggests that reactions at the core–mantle boundary might be sensitive to redox reactions at the magma–atmosphere interface.) Reaction (17) can account for at least half of Earth’s FeO content, although probably not all (Rubie et al. 2011; Fischer et al. 2015).

On sub-Neptunes, Reaction (17) suggests that magma oceans will have nonnegligible volatile-free FeO content (Wordsworth et al. 2018). The only requirement is that liquid metal and magma chemically interact during accretion.

Which of these oxidation mechanisms is more important? The FeO of Earth is less than that of Mars, even though Earth is bigger. This matches expectations for oxidation mechanism 1, but not oxidation mechanism 2. However, we have no idea whether or not this applies to exoplanets.

Appendix C Fugacity Coefficients

Our model includes nonideal behavior of H_2 and of H_2O in the atmosphere. Nonideal behavior increases the solubility of sub-Neptune atmospheric components in magma (relative to the ideal case). Although we include nonideal behavior of H_2 and of H_2O , we assume that H_2 and H_2O mix ideally. We calculated fugacity coefficients for the range 2000–3000 K and 0.01–2 GPa. We computed fugacity coefficients using both a virial EOS and the Saumon et al. (1995) EOS for H_2 , and the Haar et al. (1984) EOS based on the Helmholtz energy for H_2O .

The fugacity coefficient of a gas is related to the compressibility factor Z by the equation

$$\ln \phi = \ln \frac{f}{P} = \int_0^P \left(\frac{Z-1}{P} \right) dP, \quad (18)$$

where Z is given by

$$Z = \frac{PV_m}{RT}, \quad (19)$$

where V_m is the molar volume.

We computed H_2 fugacity coefficients using a virial EOS computed for an exponential repulsive potential (Amdur & Mason 1958; Mason & Vanderslice 1958). Only the repulsive part of the potential is important at high- T dense conditions, as discussed by Amdur & Mason (1958). The exponential repulsive potential is

$$\psi(r) = \psi_o \exp(-r\rho). \quad (20)$$

The values used for H_2 gas are $\psi_o = 10^4$ eV and $\rho = 0.204 \times 10^{-8}$ cm (Bainbridge 1962). The asymptotic limiting equations for estimating B , C , and D and the input to them are (from Henderson & Oden 1966)

$$\frac{B(T)}{b_o} = (\ln \gamma x)^3 \quad (21)$$

$$\frac{C(T)}{b_o^2} = (\ln \gamma x)^6 \quad (22)$$

$$\frac{D(T)}{b_o^3} = (\ln \gamma x)^9, \quad (23)$$

where γ is Euler’s constant and

$$x = \psi_o / kT \quad (24)$$

$$\gamma x = 206, 684, 901 / T \quad (25)$$

$$b_o = \left(\frac{2\pi N_A}{3} \right) \rho^3 = 0.0107075. \quad (26)$$

Here, N_A is Avogadro’s number.

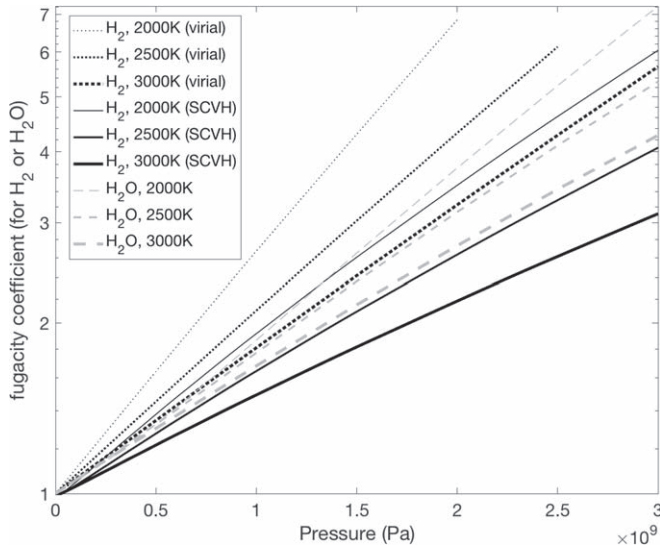


Figure 10. Fugacity coefficients. For an ideal gas, the concentration of volatiles in the magma is proportional to the partial pressure of that volatile in the atmosphere above to the magma. The fugacity coefficient corrects for the nonideality of the gas and gives the effective pressure of real gases for solubility in melts and other chemical equilibria. “SCVH” refers to the hydrogen EOS of Saumon et al. (1995). See Appendix C for details on how these fugacity coefficients were calculated.

While this approach gives good results for the range of magma–atmosphere interface conditions considered in this paper, it fails to converge above a limit roughly 0.3 of the H_2 molar volume at its critical point, i.e., about $3\times$ the molar density at the critical point.

We also calculated fugacity coefficients from the H_2 EOS tables of Saumon et al. (1995). In this calculation, we forced $Z = 1$ for $P < 10^7$ Pa (the region of significant H_2 dissociation). Using the H_2 EOS tables of Saumon et al. (1995) led to lower fugacity coefficients than the virial approach (Figure 10), implying lower importance for magma–atmosphere interactions than with the virial approach. To be conservative, we used the Saumon et al. (1995)-derived H_2 fugacities for this paper. Our conclusions in this paper are not qualitatively affected by this choice.

We computed H_2O fugacity coefficients from the Haar et al. (1984) EOS for water (the HGK EOS) as coded by Bakker (2012). Haar et al. (1984) developed an EOS based on the Helmholtz free energy of H_2O , which is valid to 2500 K and and 3 GPa. However, we used the Haar et al. EOS over the entire P – T range studied because comparisons with literature results at high P and T were reasonable (Rice & Walsh 1957; Delany & Helgeson 1978; Ostrovsky & Rizhenko 1978). For example, the HGK EOS gives molar volumes within 17% of those reported by Rice & Walsh (1957) from 0.5 to 7 GPa on the 1273 K isotherm—the highest T isotherm for which they present data. However, Wagner (2002) note Hugoniot data are not as precise as the other P – V – T data used to derive the EOS, and they did not use the data as inputs to improve the EOS at very high P and T .

Table 1 shows the H_2 virial coefficients used in this study. Figure 10 shows the H_2 and H_2O fugacity coefficients used in this study.

Table 1
 H_2 Virial Coefficients Used to Compute H_2 Fugacity Coefficients (Appendix C)

T/K	$B(H_2)$	$C(H_2)$	$D(H_2)$
2000	16.5	272	1285
2500	15.5	242	1078
3000	14.8	219	930

Appendix D Details of the Workflow

Our Section 3 workflow has four steps. Here we step through the adding- H_2 case (the adding- H_2O workflow is conceptually similar). (Step 1) We start from the initial mantle FeO content (before any H_2 has been added). From that, we find f_{O_2} (Figure 4). Then, we find the H_2/H_2O ratio of fugacities from Equations (3)–(7). We convert this to partial pressures using the fugacity coefficients in Appendix C. From the ratio of partial pressures plus the (imposed) total atmospheric pressure, we find the total mass of H_2 and of H_2O in the atmosphere. (Step 2) We then use the solubilities to figure the amounts of H_2 and of H_2O in the magma. We assume the magma is fully molten. We set an arbitrary upper limit of 25 wt% H_2O in the magma (at this upper limit, the melt is mostly H_2O in terms of mole fraction). (Step 3) Equipped with the total H_2O in the system, plus the assumption that only H_2 is initially added, the amount of FeO reduction can be figured by mass balance. Making 1 mole of H_2O requires the reduction of 1 mole of FeO. Thus, the activity of “FeO” and f_{O_2} are both lower than the initial values for H_2 addition. For mass balance purposes, we assume an activity coefficient for FeO of 1.0 (we use an FeO activity coefficient of 1.50 when calculating the f_{O_2}). We do not consider the possible effect of volatiles on the buffer equilibria (Bezmen et al. 2016). (Step 4) To make the calculation self-consistent, we iterate steps 1–3. We plug in the new value of f_{O_2} . We find the new amount of total H_2O produced (which will be lower). We recalculate the FeO decrement until convergence.

The bulk silicate Earth composition of Schaefer & Fegley (2009) is used for mass balance, except for the extreme redox end-members, where we follow the compositions of Elkins-Tanton & Seager (2008b).

Appendix E Solar System Connections

Volatile-rock reactions have long been considered as potential sources of H_2O and H_2 on Earth and Mars. Atreya et al. (1989) provide a comprehensive review, and more recent work is summarized in Dauphas & Morbidelli (2014). For example, the Fe^{2+} in Earth rocks and Mars rocks probably derives, at least in part, from the accretion of building blocks that underwent the net reaction $Fe + H_2O \rightarrow FeO + H_2$ (e.g., Ringwood 1979; Rubie et al. 2015; Appendix B). On the other hand, for Earth and Mars, nebula gas is no longer thought to have contributed much to the mass of the present-day atmospheres and oceans (e.g., Dauphas & Morbidelli 2014; but see also Olson & Sharp 2019). These Earth and Mars studies did not enforce redox balance; the H_2 must have almost entirely escaped for Earth and Mars. However, this cannot be true for sub-Neptunes.

Solar system readers should be aware that, in papers about sub-Neptunes, the “core” consists of both Fe metal and silicates, “rocky” can refer to either solid rock or liquid silicate (magma), “rocky planet” is generally taken to exclude sub-Neptunes even though Kepler sub-Neptunes are mostly silicates by mass, the terms “sub-Neptune” and “mini-Neptune” are used interchangeably, and the terms “envelope” and “atmosphere” are also used interchangeably. For sub-Neptunes, the atmosphere “gas” is mostly supercritical fluid.

ORCID iDs

Edwin S. Kite  <https://orcid.org/0000-0002-1426-1186>
 Laura Schaefer  <https://orcid.org/0000-0003-2915-5025>
 Eric B. Ford  <https://orcid.org/0000-0001-6545-639X>

References

- Abe, Y., & Matsui, T. 1986, *JGR*, **91**, E291
 Amdur, I., & Mason, E. A. 1958, *PhFl*, **1**, 370
 Anderson, G. M. 1996, *Thermodynamics of Natural Systems* (1st ed.; New York: Wiley)
 Andraut, D., Bolfan-Casanova, N., Bouhifd, M. A., et al. 2017, *PEPI*, **265**, 67
 Andraut, D., Bolfan-Casanova, N., Nigro, G. L., et al. 2011, *E&PSL*, **304**, 251
 Armstrong, K., Frost, D. J., McCammon, C. A., Rubie, D. C., & Boffa Ballaran, T. 2019, *Sci*, **365**, 903
 Atreya, S. K., Pollack, J. B., & Matthews, M. S. 1989, *Origin and Evolution of Planetary and Satellite Atmospheres* (Tucson, AZ: Univ. Arizona Press)
 Bainbridge, J. 1962, *ApJ*, **136**, 202
 Bakker, R. J. 2012, in *Thermodynamics Fundamentals and its Applications in Science*, ed. R. Morales-Rodriguez (Rijeka: InTech Open Publishing), 163
 Bali, E., Audétat, A., & Keppler, H. 2013, *Natur*, **495**, 220
 Benneke, B., Knutson, H. A., Lothringer, J., et al. 2019, *NatAs*, **3**, 813
 Benneke, B., & Seager, S. 2012, *ApJ*, **753**, 100
 Benneke, B., Wong, I., Piaulet, C., et al. 2019, *ApJ*, **887**, 14
 Bezmen, N. I., Gorbachev, P. N., & Martynenko, V. M. 2016, *Petrology*, **24**, 84
 Biersteker, J. B., & Schlichting, H. E. 2019, *MNRAS*, **485**, 4454
 Bitsch, B., Raymond, S. N., & Izidoro, A. 2019, *A&A*, **624**, A109
 Bodenheimer, P., & Lissauer, J. J. 2014, *ApJ*, **791**, 103
 Bodenheimer, P., Stevenson, D. J., Lissauer, J. J., & D’Angelo, G. 2018, *ApJ*, **868**, 138
 Bolfan-Casanova, N., Mackwell, S., Keppler, H., McCammon, C., & Rubie, D. C. 2002, *GeoRL*, **29**, 1449
 Bower, D. J., Kitzmann, D., Wolf, A. S., et al. 2019, *A&A*, **631**, A103
 Bower, D. J., Sanan, P., & Wolf, A. S. 2018, *PEPI*, **274**, 49
 Brearley, A. J. 2006, in *Meteorites and the Early Solar System II*, ed. D. S. Lauretta & H. Y. McSween (Tucson, AZ: Univ. Arizona Press), 584
 Brouwers, M. G., & Ormel, C. W. 2020, *A&A*, **634**, 15
 Brouwers, M. G., Vazan, A., & Ormel, C. W. 2018, *A&A*, **611**, A65
 Carrera, D., Ford, E. B., & Izidoro, A. 2019, *MNRAS*, **486**, 3874
 Castillo-Rogez, J., & Young, E. D. 2017, in *Planetesimals: Early Differentiation and consequences for Planets*, ed. L. T. Elkins-Tanton & B. P. Weiss (Cambridge: Cambridge Univ. Press), 92
 Chachan, Y., & Stevenson, D. J. 2018, *ApJ*, **854**, 21
 Charbonneau, D., Gaudi, B. S., Bastien, F. A., et al. 2018, *Exoplanet Science Strategy* (Washington, DC: The National Academies Press)
 Chatterjee, S., & Tan, J. C. 2014, *ApJ*, **780**, 53
 Chen, H., & Rogers, L. A. 2016, *ApJ*, **831**, 180
 Chiang, E., & Laughlin, G. 2013, *MNRAS*, **431**, 3444
 Clesi, V., Bouhifd, M. A., Bolfan-Casanova, N., et al. 2018, *SciA*, **4**, e1701876
 Cossou, C., Raymond, S. N., Hersant, F., et al. 2014, *A&A*, **569**, A56
 Crossfield, I. J. M., & Kreidberg, L. 2017, *AJ*, **154**, 261
 Dasgupta, R., & Grawal, D. S. 2019, *Deep Carbon: Past to Present* (Cambridge: Cambridge Univ. Press), 4
 Dauphas, N., & Morbidelli, A. 2014, in *Treatise on Geochemistry*, ed. H. D. Holland & K. K. Turekian (2nd ed.; Oxford: Elsevier), 1
 David, T. J., Petigura, A. E., Luger, R., Foreman-Mackey, D., et al. 2019, *ApJL*, **885**, L12
 Deguen, R., Landeau, M., & Olson, P. 2014, *E&PSL*, **391**, 274
 Delany, J. M., & Helgeson, H. C. 1978, *AmJS*, **278**, 638
 Doyle, A. E., Young, E. D., Klein, B., Zuckerman, B., & Schlichting, H. E. 2019, *Sci*, **366**, 356
 Dragomir, D., Matthews, J. M., Eastman, J. D., et al. 2013, *ApJL*, **772**, L2
 Dzierwonski, A. M., & Anderson, D. L. 1981, *PEPI*, **25**, 297
 Elkins-Tanton, L. T. 2011, *Ap&SS*, **332**, 359
 Elkins-Tanton, L. T. 2012, *AREPS*, **40**, 113
 Elkins-Tanton, L. T., & Seager, S. 2008a, *ApJ*, **685**, 1237
 Elkins-Tanton, L. T., & Seager, S. 2008b, *ApJ*, **688**, 628
 European Space Agency 2013, *PLATO: Revealing Habitable Worlds Around Solar-like Stars*, Assessment Study Report, ESA/SRE(2013)5
 Fegley, B. 2013, *Practical Chemical Thermodynamics For Geoscientists* (Oxford: Elsevier)
 Fegley, B., Jr., Jacobson, N. S., Williams, K. B., et al. 2016, *ApJ*, **824**, 103
 Fegley, B., Jr., & Schaefer, L. 2014, in *Treatise on Geochemistry*, ed. K. Turekian & H. Holland (2nd ed.; Amsterdam: Elsevier), 127
 Fischer, R. A., Campbell, A. J., & Ciesla, F. J. 2017, *EPSL*, **458**, 252
 Fischer, R. A., Nakajima, Y., Campbell, A. J., et al. 2015, *GeCoA*, **167**, 177
 Fortney, J. J., Mordasini, C., Nettelmann, N., et al. 2013, *ApJ*, **775**, 80
 Fraine, J., Deming, D., Benneke, B., et al. 2014, *Natur*, **513**, 526
 French, M., & Nettelmann, N. 2019, *ApJ*, **881**, 81
 Frost, D. J., Liebske, C., Langenhorst, F., et al. 2004, *Natur*, **428**, 409
 Frost, D. J., Mann, U., Asahara, Y., & Rubie, D. C. 2008, *RSPTA*, **366**, 4315
 Fulton, B. J., & Petigura, E. A. 2018, *AJ*, **156**, 264
 Fulton, B. J., Petigura, E. A., Howard, A. W., et al. 2017, *AJ*, **154**, 109
 Garaud, P. 2018, *AnRFM*, **50**, 275
 Genda, H., Iizuka, T., Sasaki, T., Ueno, Y., & Ikoma, M. 2017, *E&PSL*, **470**, 87
 Ginzburg, S., Schlichting, H. E., & Sari, R. 2016, *ApJ*, **825**, 29
 Ginzburg, S., Schlichting, H. E., & Sari, R. 2018, *MNRAS*, **476**, 759
 Glushko, V. P., Medvedev, V. A., Gurvich, L. V., & Yungman, V. S. 1999, *Thermal Constants of Substances* (New York: Wiley)
 Gounelle, M. 2015, *A&A*, **582**, A26
 Grossman, L., Fedkin, A. V., & Simon, S. B. 2012, *M&PS*, **47**, 2160
 Haar, L., Gallagher, J. S., & Kell, G. S. 1984, *NBS/NRC Steam Tables* (Washington, DC: Hemisphere Publishing)
 Haberle, R. M., Zahnle, K., Barlow, N. G., et al. 2019, *GeoRL*, **46**, 13355
 Hamano, K., Abe, Y., & Genda, H. 2013, *Natur*, **497**, 607
 Helled, R., & Stevenson, D. 2017, *ApJL*, **840**, L4
 Henderson, D., & Oden, L. 1966, *PhFl*, **9**, 1592
 Hernlund, J. W. 2016, in *Deep Earth: Physics and Chemistry of the Lower Mantle and Core*, ed. R. Fischer & H. Terasaki (Washington, DC: AGU), 201
 Hirose, K., Tagawa, S., Kuwayama, Y., et al. 2019, *GeoRL*, **46**, 5190
 Hirschmann, M. M. 2012, *E&PSL*, **341**, 48
 Hirschmann, M. M., Withers, A. C., Ardia, P., & Foley, N. T. 2012, *E&PSL*, **345**, 38
 Holzheid, A., Palme, H., & Chakraborty, S. 1997, *ChGeo*, **139**, 21
 Howe, A. R., & Burrows, A. 2015, *ApJ*, **808**, 150
 Hsu, D. C., Ford, E. B., Ragozzine, D., & Ashby, K. 2019, *AJ*, **158**, 109
 Huang, C. X., Burt, J., Vanderburg, A., et al. 2018, *ApJL*, **868**, L39
 Ikoma, M., Elkins-Tanton, L., Hamano, K., & Suckale, J. 2018, *SSRv*, **214**, 76
 Ikoma, M., & Genda, H. 2006, *ApJ*, **648**, 696
 Inamdar, N. K., & Schlichting, H. E. 2015, *MNRAS*, **448**, 1751
 Inamdar, N. K., & Schlichting, H. E. 2016, *ApJ*, **817**, L13
 Izidoro, A., Ogihara, M., Raymond, S. N., et al. 2017, *MNRAS*, **470**, 1750
 Javoy, M. 1995, *GeoRL*, **22**, 2219
 Johnson, J. A., Petigura, E. A., Fulton, B. J., et al. 2017, *AJ*, **154**, 108
 Karki, B. B., Bhattarai, D., Mookherjee, M., & Stixrude, L. 2010, *PCM*, **37**, 103
 Katz, R. F., Spiegelman, M., & Langmuir, C. H. 2003, *GGG*, **4**, 1073
 Khurana, K. K., Jia, X., Kivelson, M. G., et al. 2011, *Sci*, **332**, 1186
 Kite, E. S., Fegley, B., Schaefer, L., & Ford, E. B. 2019, *ApJL*, **87**, L33
 Kite, E. S., Fegley, B., Jr., Schaefer, L., & Gaidos, E. 2016, *ApJ*, **828**, 80
 Kite, E. S., & Ford, E. B. 2018, *ApJ*, **864**, 75
 Kite, E. S., Manga, M., & Gaidos, E. 2009, *ApJ*, **700**, 1732
 Klein, F., Bach, W., & McCollom, T. M. 2013, *Litho*, **178**, 55
 Knutson, H. A., Dragomir, D., Kreidberg, L., et al. 2014, *ApJ*, **794**, 155
 Komabayashi, T. 2014, *JGRB*, **119**, 4164
 Kowalski, M., & Spencer, P. J. 1995, *Calphad*, **19**, 229
 Kress, V. C., & Carmichael, I. S. E. 1991, *CoMP*, **108**, 82
 Krot, A. N., Fegley, B., Jr., Lodders, K., & Palme, H. 2000, in *Protostars and Planets IV*, ed. V. Mannings, A. P. Boss, & S. S. Russell (Tucson, AZ: Univ. Arizona Press), 1019
 Lange, M. A., & Ahrens, T. J. 1984, *E&PSL*, **71**, 111
 Le Guillou, C., Changela, H. G., & Brearley, A. J. 2015, *E&PSL*, **420**, 162
 Leconte, J., & Chabrier, G. 2012, *A&A*, **540**, A20

- Lee, E. J. 2019, *ApJ*, **878**, 36
- Lee, E. J., Chiang, E., & Ferguson, J. W. 2018, *MNRAS*, **476**, 2199
- Léger, A., Grasset, O., Fegley, B., et al. 2011, *Icar*, **213**, 1
- Levison, H. F., Kretke, K. A., Walsh, K. J., & Bottke, W. F. 2015, *PNAS*, **112**, 14180
- Lewis, J. S. 2004, *Physics and Chemistry of the Solar System* (2nd ed.; Amsterdam: Elsevier)
- Lichtenberg, T., Golabek, G. J., Burn, R., et al. 2019, *NatAs*, **3**, 307
- Liu, S.-F., Hori, Y., Müller, S., et al. 2019, *Natur*, **572**, 355
- Lopez, E. D., & Fortney, J. J. 2014, *ApJ*, **792**, 1
- Mann, A. W., Gaidos, E., Vanderburg, A., et al. 2017, *AJ*, **153**, 64
- Mason, E. A., & Vanderslice, J. T. 1958, *JChPh*, **28**, 432
- Massol, H., Hamano, K., Tian, F., et al. 2016, *SSRv*, **205**, 153
- McCollom, T. M., & Bach, W. 2009, *GeCoA*, **73**, 856
- Miyazaki, Y., & Korenaga, J. 2019, *JGRB*, **124**, 3399
- Mordasini, C. 2018, *Handbook of Exoplanets* (Cham: Springer), 143
- Mordasini, C., van Boekel, R., Mollière, P., Henning, T., & Benneke, B. 2016, *ApJ*, **832**, 41
- Morley, C. V., Knutson, H., Line, M., et al. 2017, *AJ*, **153**, 86
- Morley, C. V., Skemer, A. J., Miles, B. E., et al. 2019, *ApJL*, **882**, L29
- Nettelmann, N., Fortney, J. J., Kramm, U., & Redmer, R. 2011, *ApJ*, **733**, 2
- Newton, E. R., Mann, A. W., Tofflemire, B. M., et al. 2019, *ApJL*, **880**, L17
- Ni, H., Zhang, L., Xiong, X., Mao, Z., & Wang, J. 2017, *ESRv*, **167**, 62
- Nittler, L. R., Chabot, N. L., Grove, T. L., & Peplowski, P. N. 2017, arXiv:1712.02187
- Ochs, F. A., & Lange, R. A. 1999, *Sci*, **283**, 1314
- Ogihara, M., Morbidelli, A., & Guillot, T. 2015, *A&A*, **578**, A36
- Olson, P. L., & Sharp, Z. D. 2019, *PEPI*, **294**, 106294
- Ormel, C. W., Shi, J.-M., & Kuiper, R. 2015, *MNRAS*, **447**, 3512
- Ostrovsky, I. A., & Rizhenko, B. N. 1978, *PCM*, **2**, 297
- Owen, J. E. 2019, *AREPS*, **47**, 67
- Owen, J. E., & Wu, Y. 2017, *ApJ*, **847**, 29
- Pahlevan, K., Schaefer, L., & Hirschmann, M. M. 2019, *EPSL*, **526**, 115770
- Papale, P. 1997, *CoMP*, **126**, 237
- Pöhlmann, M., Benoit, M., & Kob, W. 2004, *PhRvB*, **70**, 184209
- Putirka, K. D., & Rarick, J. C. 2019, *AmMin*, **104**, 817
- Raymond, S. N., Boulet, T., Izidoro, A., Esteves, L., & Bitsch, B. 2018, *MNRAS*, **479**, L81
- Rice, K., Malavolta, L., Mayo, A., et al. 2019, *MNRAS*, **484**, 3731
- Rice, M. H., & Walsh, J. M. 1957, *JChPh*, **26**, 824
- Righter, K., & O'Brien, D. P. 2011, *PNAS*, **108**, 19165
- Ringwood, A. E. 1979, *Origin of the Earth and Moon* (New York: Springer)
- Rogers, L. A. 2015, *ApJ*, **801**, 41
- Rogers, L. A., Bodenheimer, P., Lissauer, J. J., & Seager, S. 2011, *ApJ*, **738**, 59
- Rogers, L. A., & Seager, S. 2010, *ApJ*, **716**, 1208
- Rosenberg, N. D., Browning, L., & Bourcier, W. L. 2001, *M&PS*, **36**, 239
- Rubie, D. C., Frost, D. J., Mann, U., et al. 2011, *EPSL*, **301**, 31
- Rubie, D. C., Jacobson, S. A., Morbidelli, A., et al. 2015, *Icar*, **248**, 89
- Sasaki, S. 1990, in *The Primary Solar-type Atmosphere Surrounding the Accreting Earth: H₂O-induced High Surface Temperature*, ed. H. Newsom & J. H. Jones (Oxford: Oxford Univ. Press), 195
- Saumon, D., Chabrier, G., & van Horn, H. M. 1995, *ApJS*, **99**, 713
- Schaefer, L., & Elkins-Tanton, L. T. 2018, *RSPTA*, **376**, 20180109
- Schaefer, L., & Fegley, B. 2009, *ApJL*, **703**, L113
- Schaefer, L., & Fegley, B. 2010, *Icar*, **208**, 438
- Schaefer, L., & Fegley, B. 2017, *ApJ*, **843**, 120
- Schaefer, L., Wordsworth, R. D., Berta-Thompson, Z., & Sasselov, D. 2016, *ApJ*, **829**, 63
- Seward, T. M., & Franck, E. U. 2019, *Ber. Bunsenges. Phys. Chem*, **85**, 27
- Shen, A. H., & Keppler, H. 1997, *Natur*, **385**, 710
- Silva Aguirre, V., Davies, G. R., Basu, S., et al. 2015, *MNRAS*, **452**, 2127
- Sleep, N. H., Meibom, A., Fridriksson, T., Coleman, R. G., & Bird, D. K. 2004, *PNAS*, **101**, 12818
- Sossi, P. A., & Fegley, B. 2018, *RvMG*, **84**, 393
- Soubiran, F., & Militzer, B. 2015, *ApJ*, **806**, 228
- Stevenson, D. J. 1977, *Natur*, **268**, 130
- Stevenson, D. J. 1984, *LPICo*, **540**, 60
- Stolper, E. 1982, *GeCoA*, **46**, 2609
- Tinetti, G., Drossart, P., Eccleston, P., et al. 2016, *Proc. SPIE*, **9904**, 99041X
- Turrini, D., Miguel, Y., Zingales, T., et al. 2018, *ExA*, **46**, 45
- Unterborn, C. T., Hull, S. D., Stixrude, L., et al. 2017, *LPICo*, **2042**, 4034
- Urey, H. 1952, *The Planets: Their Origin and Development* (New Haven, CT: Yale Univ. Press)
- Valencia, D., O'Connell, R. J., & Sasselov, D. 2006, *Icar*, **181**, 545
- Van Eylen, V., Agentoft, C., Lundkvist, M. S., et al. 2018, *MNRAS*, **479**, 4786
- Van Grootel, V., Gillon, M., Valencia, D., et al. 2014, *ApJ*, **786**, 2
- Vanderburg, A., Huang, C. X., Rodriguez, J. E., et al. 2019, *ApJL*, **881**, L19
- Vazan, A., Ormel, C. W., & Dominik, C. 2018a, *A&A*, **610**, L1
- Vazan, A., Ormel, C. W., Noack, L., & Dominik, C. 2018b, *ApJ*, **869**, 163
- Venturini, J., & Helled, R. 2017, *ApJ*, **848**, 95
- Wagner, W., & Pruß, A. 2002, *JPCRD*, **31**, 387
- Wahl, S. M., Hubbard, W. B., Militzer, B., et al. 2017, *GeoRL*, **44**, 4649
- Wakeford, H. R., Sing, D. K., Kataria, T., et al. 2017, *Sci*, **356**, 628
- Wänke, H. 1981, *RSPTA*, **303**, 287
- Wilson, L., Keil, K., Browning, L. B., Krot, A. N., & Bourcier, W. 1999, *M&PS*, **34**, 541
- Winn, J. N., Sanchis-Ojeda, R., & Rappaport, S. 2018, *NewAR*, **83**, 37
- Wolfgang, A., Rogers, L. A., & Ford, E. B. 2016, *ApJ*, **825**, 19
- Wordsworth, R. D., Schaefer, L. K., & Fischer, R. A. 2018, *AJ*, **155**, 195
- Wu, J., Desch, S. J., Schaefer, L., et al. 2018, *JGRE*, **123**, 2691
- Young, E. 2020, *IAU Symp. 345 in Origins: From the Protosun to the First Steps of Life* (Cambridge: Cambridge Univ. Press), 70
- Zahnle, K. J., & Catling, D. C. 2017, *ApJ*, **843**, 122
- Zhang, H. L., Hirschmann, M. M., Cottrell, E., & Withers, A. C. 2017, *GeCoA*, **204**, 83
- Zolensky, M. E., Bourcier, W. L., & Gooding, J. L. 1989, *Icar*, **78**, 411
- Zolensky, M. E., Krot, A. N., & Benedix, G. 2008, *RvMG*, **68**, 429